High throughput evaluation of genetic variants with prime editing sensor libraries

Samuel I. Gould[1,2], Alexandra N. Wuest[1,2], Kexin Dong[2,3], Grace A. Johnson[1,2], Alvin Hsu[4,5,6], Varun K. Narendra[7], Stuart S. Levine[1,2], David R. Liu[4,5,6], Francisco J. Sánchez Rivera[1,2,#].

[1]Department of Biology, Massachusetts Institute of Technology, Cambridge, 02142, Massachusetts, USA.

[2]David H. Koch Institute for Integrative Cancer Research, Massachusetts Institute of Technology, Cambridge, 02142, Massachusetts, USA.

[3]University of Chinese Academy of Sciences, Beijing, China.

[4]Merkin Institute of Transformative Technologies in Healthcare, Broad Institute of MIT and Harvard, Cambridge, MA, USA.

[5]Department of Chemistry and Chemical Biology, Harvard University, Cambridge, MA, USA.

[6]Howard Hughes Medical Institute, Harvard University, Cambridge, MA, USA.

[7]Cancer Biology and Genetics Program, Memorial Sloan Kettering Cancer Center, New York, NY 10065, USA.

[#]Correspondence: fsr@mit.edu

Abstract

Many human diseases have a strong association with diverse types of genetic alterations. These diseases include cancer, in which tumor genomes often harbor a complex spectrum of single-nucleotide alterations and chromosomal rearrangements that can perturb gene function in ways that remain poorly understood. Some cancer-associated genes exhibit a tremendous degree of mutational heterogeneity, which may impact disease initiation, progression, and therapy responses. For example, *TP53*, the most frequently mutated gene in cancer, shows extensive allelic variation that leads to the generation of altered proteins that can produce functionally distinct phenotypes. Whether distinct variants of *TP53* and other genes encode proteins with loss-of-function, gain-of-function, or otherwise neomorphic phenotypes remains both controversial and technically challenging to assess, particularly at the endogenous level. Here, we present a high-throughput prime editing “sensor” strategy to quantitatively assess the functional impact of diverse types of endogenous genetic variants. We used this strategy to screen the largest collection of endogenous cancer-associated *TP53* variants assembled to date, identifying both known and novel alleles that impact p53 function in mechanistically diverse ways. Intriguingly, we find that certain types of endogenous *TP53* variants, particularly those in the p53 oligomerization domain, display opposite phenotypes in exogenous overexpression systems. These include disease-relevant variants

found in humans with cancer predisposition syndromes that encode altered proteins with unique molecular properties. Our results emphasize the physiological importance of gene dosage in shaping native protein stoichiometry and protein-protein interactions, highlight the dangers of using exogenous overexpression systems to interpret pathogenic alleles, and establish a powerful computational and experimental framework for studying diverse types of genetic variants in their endogenous sequence context at scale.

Introduction

A wide range of human diseases are associated with diverse genetic alterations that may be responsible for initiating, promoting, or otherwise modifying the course of a given disease. These alterations can be quite complex; for instance, cancer genomes typically contain a repertoire of single nucleotide variants (SNVs) and large-scale copy number alterations (CNAs) that can impact many genes in different ways depending on the type of alteration, gene function, and biological context. While tumor genotype is a well-established determinant of disease initiation, progression, and therapy responses, the functional impact conferred by the thousands of unique mutations observed in human tumors remains poorly understood. This presents a major challenge to precision medicine efforts that aim to tailor cancer therapies to patients suffering from cancers harboring specific genetic lesions. Beyond the clinic, understanding the impact that diverse types of mutations have on different residues and protein domains would improve our fundamental understanding of gene and protein function **(Fig. 1a)**.

Until recently, approaches for studying genetic variants have been limited to low-throughput, homology-directed repair (HDR) based methods or high-throughput, non-physiological gene overexpression systems[1–7]. While powerful, the former approach lacks scalability and generality due to the requirements of HDR and its limitation primarily to actively dividing cells. Gene overexpression systems have fewer requirements and are scalable but fail to physiologically recapitulate the biology driven by these variants due to the absence of endogenous gene regulation mechanisms, many of which are not known for genes of interest. The recent development of precision genome editing tools, including base editing and prime editing, allows variants to be modeled in their native endogenous genomic context with increased editing efficiency and theoretically higher throughput[8–10].

55 Prime editing[10] can be used to generate effectively any type of small mutation, including all SNVs and small
56 insertions and deletions (indels). Prime editors are directed to engineer a mutation of interest by the instructions
57 encoded in a prime editing guide RNA (pegRNA), which contains both a protospacer (the "search" sequence)
58 and a 3' extension sequence (the "replace" sequence that dictates the mutation installed at the site). The modular
59 search-and-replace ability of prime editing has been leveraged to interrogate endogenous variants in high-
60 throughput[11–13]. In these approaches, libraries of pegRNAs are transiently or stably delivered to cells expressing
61 prime editors, and the fitness of variants is assessed by determining the relative distribution of endogenous
62 alleles and/or pegRNAs. While powerful, these approaches have important limitations for screening applications,
63 including 1) reliance on a small number of variant-specific pegRNAs with unknown editing performance, 2)
64 inability to quantitatively assess endogenous genome editing at scale, and 3) potential overrepresentation of
65 undesired indels due to using PE3.

66 With these challenges in mind, we sought to develop an integrative computational and experimental framework
67 for high-throughput design, screening, and deconvolution of pegRNA libraries to interrogate a diverse spectrum
68 of genetic variants. This includes pairing each pegRNA with a variant-specific synthetic "sensor" site[14] that
69 recapitulates the native architecture of the endogenous target locus. Doing so allows linkage of pegRNA identity
70 to editing outcomes for simultaneous high-throughput quantification of pegRNA editing activity and empirical
71 calibration of screening data.

72 We chose the p53 transcription factor as a prototype to test the utility of this approach for investigating the
73 biological impact of specific genetic variants. Notably, *TP53* is the most frequently mutated gene in cancer and
74 exhibits significant allelic variation, leading to the generation of altered proteins that can produce functionally
75 distinct phenotypes. Whether distinct variants of *TP53* and other genes encode proteins with loss-of-function,
76 gain-of-function, or otherwise neomorphic activities that influence cancer phenotypes is both controversial and
77 technically challenging to investigate, particularly in high-throughput. Multiple studies have used cDNA-based
78 exogenous overexpression systems to probe the fitness of p53 variants in human, mouse, and yeast
79 systems[6,7,15,16]. However, given the artificial nature of these screens, which rely on expression of variants at
80 supraphysiological levels, we hypothesized that these screens could have misrepresented one or more

81 phenotypes associated with p53 variants. Artifacts that stem from exogenous overexpression systems could be
82 particularly relevant when studying proteins like p53 because p53 functions as a tetramer whose expression and
83 degradation is tightly controlled by the cell[17–19]. Thus, we reasoned that alterations to the stoichiometric balance
84 of p53 via overexpression could lead to erroneous conclusions about the effects of particular p53 variants,
85 including mis-classifying certain variants as non-causal or otherwise benign.

86 To tackle this question, we generated and screened a library of >28,000 pegRNAs targeting >1,000 *TP53*
87 variants observed across >40,000 cancer patients[20] — the largest set of endogenous *TP53* variants studied to
88 date. We included SNVs, insertions, and deletions observed in patients, putative neutral silent substitutions as
89 controls, and a panel of random indels to increase the functional search space. These experiments identified
90 both known and novel alleles that impact p53 function in mechanistically diverse ways. Intriguingly, we
91 discovered that certain types of endogenous variants, particularly those found in the p53 oligomerization domain,
92 display opposite phenotypes when tested with exogenous overexpression systems. Collectively, these results
93 highlight the physiological importance of gene dosage in shaping native protein stoichiometry and protein-protein
94 interactions, and establish a powerful computational and experimental framework for studying diverse types of
95 genetic variants at scale. To ensure widespread accessibility of this resource for the scientific community, we
96 provide a publicly available Python package, Prime Editing Guide Generator (pegg.readthedocs.io), as a tool to
97 generate prime editing sensor libraries.

98 **Results:**

99 **High-throughput design of prime editing sensor libraries with Prime Editing Guide Generator (PEGG)**

100 A major limitation of using prime editing to systematically investigate genetic variants is the inherent variability
101 in editing efficiency among different pegRNAs[10,21–23]. A number of computational tools for pegRNA design have
102 been developed[24–33], including machine learning algorithms that can nominate sets of pegRNAs predicted to
103 produce high efficiency edits. However, even pegRNAs generated by these predictive algorithms require
104 extensive experimental validation, and their editing activity is not guaranteed to correlate strongly across different
105 cell types. We hypothesized that coupling pegRNAs with “sensors”—artificial copies of their endogenous target

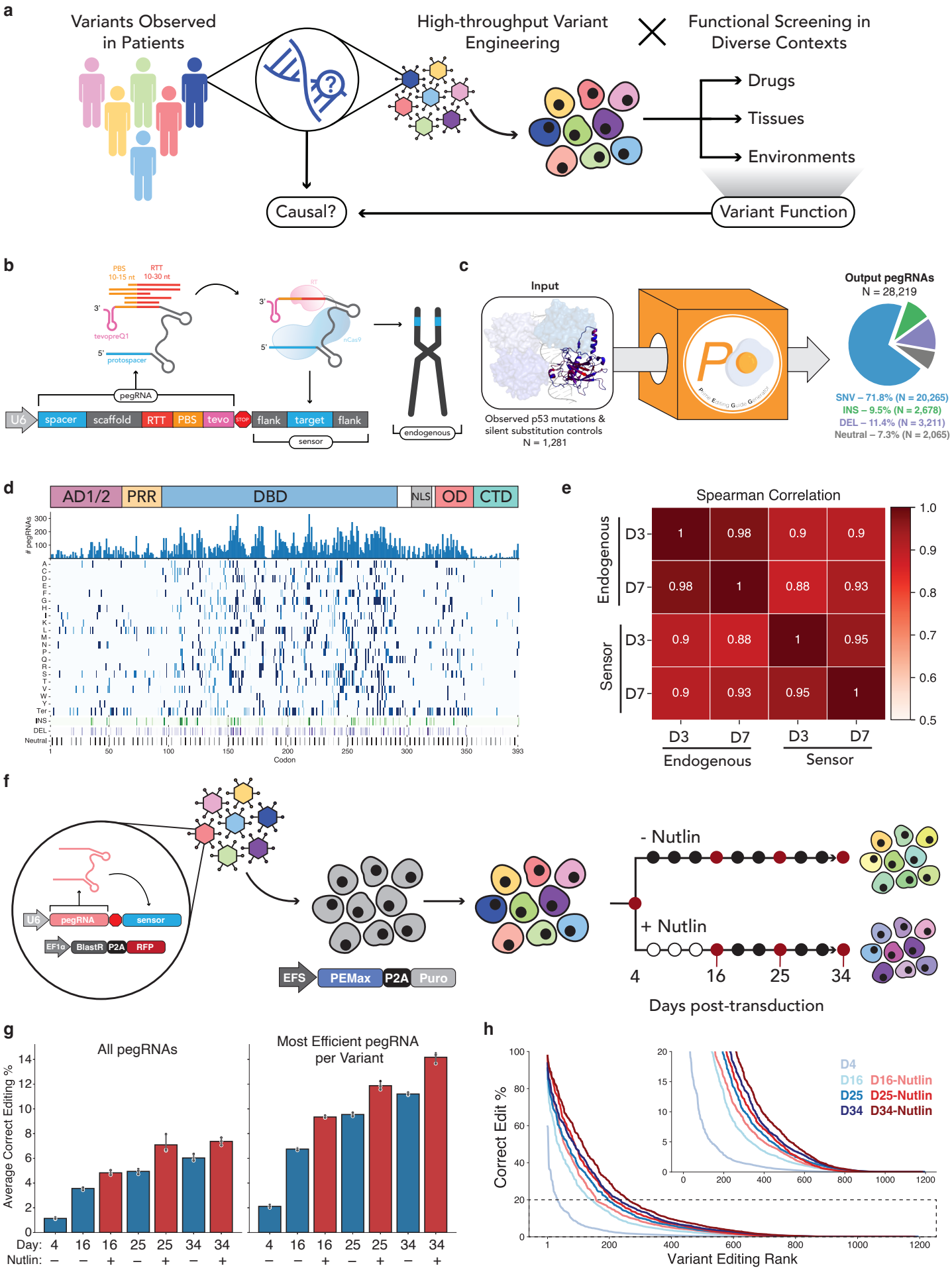
a
Variants Observed in Patients
High-throughput Variant Engineering
Functional Screening in Diverse Contexts
Drugs
Tissues
Environments
Causal?
Variant Function
b
PBS 10-15 nt
RTT 10-30 nt
tevopreQ1
protospacer
pegRNA
U6
spacer
scaffold
RTT
PBS
tevo
STOP
flank
target
flank
sensor
nCas9
endogenous
c
Input
Observed p53 mutations & silent substitution controls N = 1,281
Output pegRNAs
N = 28,219
SNV – 71.8% (N = 20,265)
INS – 9.5% (N = 2,678)
DEL – 11.4% (N = 3,211)
Neutral – 7.3% (N = 2,065)
d
AD1/2
PRR
DBD
NLS
OD
CTD
pegRNAs
Codon
e
Spearman Correlation
Endogenous
Sensor
D3
D7
1
0.98
0.9
0.9
0.98
1
0.88
0.93
0.9
0.88
1
0.95
0.9
0.93
0.95
1
f
U6
pegRNA
sensor
EF1α
BlastR
P2A
RFP
EFS
PEMax
P2A
Puro
- Nutlin
+ Nutlin
4
16
25
34
Days post-transduction
g
All pegRNAs
Most Efficient pegRNA per Variant
Average Correct Editing %
Day: 4 16 16 25 25 34 34
Nutlin: – – + – + – +
h
Correct Edit %
Variant Editing Rank
D4
D16
D16-Nutlin
D25
D25-Nutlin
D34
D34-Nutlin

Fig. 1 | High Throughput design and evaluation of a *TP53* prime editing sensor library. a, Schematic of our overall approach. We aim to engineer variants observed in patients with high-throughput to perform functional screens in diverse contexts, elucidating variant functions to improve our ability to stratify and treat patients. **b,** Schematic of the sensor framework, which links each pegRNA to its editing outcome at the endogenous locus. RTT = reverse transcription template, PBS = primer binding site, tevo = tevopreQ1, RT = reverse transcriptase, nCas9 = nicking Cas9. **c,** We used PEGG to generate a *TP53* prime editing sensor library targeting over a thousand cancer-associated *TP53* variants with a median of 30 pegRNAs per variant. **d,** Heatmap visualization of the pegRNAs included in the *TP53* sensor library, which includes SNVs, indels, and silent substitutions. AD1/2 = activation domain 1/2, PRR = proline rich region, DBD = DNA binding domain, NLS = nuclear localization signal, OD = oligomerization domain, CTD = C-terminal domain. **e,** Correlation between editing at the sensor and endogenous locus in 8 *TP53*-targeting pegRNA-sensor pairs at Day 3 (D3) and Day 7 (D7) post-transduction. **f,** Schematic of the screening protocol. The prime editing sensor library is transduced into cells constitutively expressing PEmax, and screening is performed in the presence or absence of the small molecule Nutlin-3. **g,** The average correct editing percentage among all pegRNAs in the library (left) or when considering only the most efficient pegRNA for each variant (right) at various time-points in both conditions. **h,** Rank plot of the correct editing percentage of the most efficient pegRNA per variant, as assayed at the sensor locus, at each time-point.

106 sites—would allow us to systematically identify high efficiency pegRNAs while controlling for the confounding
107 effects of variable editing efficiency in a screening context **(Fig. 1b)**.

108 Synthetic sensor-like target sites have been previously used by our group and others to control for base editing
109 gRNA editing efficiencies while defining the relative fitness of variants in genetic screens[14,34]. Multiple studies
110 have applied a similar strategy to both base and prime editing technologies to identify features of efficient gRNAs
111 or pegRNAs and train predictive algorithms[21,32,33,35–37]. However, this approach has yet to be applied for high-
112 throughput phenotypic screening of endogenous genetic variants with prime editing, likely due in part to the lower
113 editing efficiency of prime editing relative to base editing. We reasoned that a sensor-based prime editing
114 screening approach could be powerful to discriminate *bona fide* endogenous variants from undesired editing
115 outcomes that enrich or deplete in a screen. Moreover, the sensor approach would theoretically overcome the
116 limitations of assessing variants at different genetic sites in parallel by eliminating the need to sequence multiple
117 endogenous loci.

118 To test this approach, we first needed to build a computational tool capable of designing and ranking pegRNAs
119 for thousands of genetic variants, while automatically generating a paired sensor site. To address this unmet
120 need, we built and publicly released the Prime Editing Guide Generator (PEGG) **(Extended Data Fig. 1a)**, a
121 Python package that enables high throughput design of prime editing sensor libraries[38] (available at
122 pegg.readthedocs.io). PEGG is compatible with a range of mutation input formats, including all of the datasets
123 on the cBioPortal, ClinVar identifiers, and custom mutation inputs[39,40].

124 We chose the *TP53* tumor suppressor gene as a prototype to establish and credential a scalable prime editing
125 sensor-based screening approach for a number of reasons. First, *TP53* is the most frequently mutated gene in
126 human cancer, with ~50% of patients suffering from tumors harboring a mutation within the *TP53* gene while the
127 rest often inactivate the p53 pathway through other mechanisms. Secondly, thousands of unique *TP53* mutations
128 have been identified in cancer patients, including eight or so “hotspot” alleles in specific residues that exhibit the
129 highest mutational frequencies[19]. Although p53 has been studied for decades, there have been few systematic
130 studies, and those have been hampered by reliance on artificial overexpression of mutant p53 proteins,
131 unrepresentative cell lines, and/or a limited spectrum of mutations evaluated[6,7,15,16]. These and other studies

132 have sparked controversy in the field over whether any mutant p53 proteins are endowed with activities that go
133 beyond loss-of-function or dominant negative activity to achieve gain-of-function or neomorphic status. These
134 are important questions that extend beyond *TP53* because mutant gain-of-function proteins generated by
135 cancer-associated variants, and the phenotypes they produce, could represent attractive therapeutic targets.
136 Lastly, prime editing sensor-based screening could be scaled up and broadly deployed to identify causal genetic
137 variants implicated in cancer and other diseases with a strong genetic association.

138 With the above goals in mind, we first sought to generate a library of pegRNAs targeting *TP53* variants. To
139 generate this library, we selected variants from the MSK-IMPACT database, which uses deep exon sequencing
140 of patient tumor samples to identify cancer-associated variants[20]. From this database of over 40,000 patients,
141 we chose all observed SNVs in p53, as well as frequently observed insertions and deletions, along with a
142 collection of random indels **(Extended Data Fig. 1b)**. We reasoned that including multiple pegRNAs with different
143 protospacers and combinations of pegRNA properties for each variant would allow us to scan the pegRNA design
144 space more thoroughly to identify highly efficient guides for robust statistical analysis of variant phenotypes. To
145 accomplish this, we used PEGG to produce 30 pegRNA designs per variant (for pegRNAs with a sufficient
146 number of accessible PAM sequences) with varying RTT (10–30 nt) and PBS lengths (10–15 nt) coupled to
147 canonical "NGG" protospacers. The generated pegRNA designs were ranked based on a composite "PEGG
148 score" that integrates literature best practices for pegRNA design **(Extended Data Fig. 1a, Supplemental Table
149 1)**.

150 PEGG also generated silent substitution variants as neutral internal controls for the screen. We also filtered
151 pegRNAs to exclude protospacers with an MIT specificity score below 50 to reduce the probability of off-target
152 editing[41] **(Extended Data Fig. 1e)**. In addition, these pegRNA designs included an epegRNA motif, tevopreQ$_1$,
153 an RNA pseudoknot located at the 3′ end of the pegRNA that improves editing by preventing degradation of the
154 guide[22]. Even after these relatively stringent filtration steps, we were able to generate pegRNA designs for more
155 than 95% of the input variants, resulting in a library of >28,000 pegRNAs **(Fig. 1c, 1d; Extended Data Fig. 1c,
156 1d)**. Each pegRNA in the library is also paired with a 60-nucleotide long variant-specific synthetic "sensor" that

157 is generated by PEGG and included in the final oligonucleotide design. Every sensor is designed to recapitulate
158 the native endogenous target locus, thereby linking pegRNA identity to editing outcomes **(Fig. 1b)**.

159 To test the efficacy of using the sensor as a readout of editing at the endogenous locus, we randomly selected
160 eight *TP53* variant-specific pegRNA sensors generated during the process of library preparation. We generated
161 lentivirus for each of these PE sensor constructs and performed separate transductions into cells expressing
162 PEmax. At 3- and 7-days post-transduction, we harvested genomic DNA and amplified both the pegRNA–sensor
163 cassette and the endogenous locus targeted by each pegRNA. Analysis of editing at the sensor and endogenous
164 locus revealed a very high correlation between the sensors and endogenous sites (Spearman correlation ≥ 0.9;
165 **Fig. 1e**). In general, the prime editing sensor seems to slightly overestimate the editing activity at the endogenous
166 locus, likely in part due to differences in locus chromatin accessibility[42], but the ranking of pegRNA editing
167 efficiencies is largely preserved, validating our sensor-based approach.

168 **High-throughput interrogation of *TP53* variants using prime editing sensor libraries**

169 Next, we screened these variants in *TP53* WT A549 lung adenocarcinoma cells stably expressing PEmax[21]. To
170 measure prime editing activity, we generated and transduced these cells with a modified all-in-one lentiviral
171 version of the fluorescence-based PEAR reporter[43], which displayed strong editing activity **(Extended Data Fig.
172 2a)**. We then introduced the lentiviral *TP53* sensor library into these cells at a low multiplicity of infection and in
173 triplicate while ensuring a library representation of >1000X at every step of the screen. Four days post-
174 transduction, we split the populations into untreated or Nutlin-3-treatment arms **(Fig. 1f)**. Nutlin-3 is a small
175 molecule that inhibits MDM2 to activate the p53 pathway, and some *TP53* mutations have been shown to
176 promote bypass of p53-dependent cell cycle arrest and apoptosis[44]. We hypothesized that this treatment group
177 may increase the signal-to-noise ratio between *TP53* variants with loss-of-function (LOF) and gain-of-function
178 (GOF) activities. We allowed the screen to progress for 34 days, harvesting cell pellets from each replicate and
179 treatment arm at multiple time-points **(Extended Data Fig. 2b)**. Genomic DNA extracted from each sample was
180 used to amplify the pegRNA–sensor cassettes, which were subjected to next-generation sequencing to
181 simultaneously assess enrichment/depletion of pegRNAs and their editing activity and outcomes at the sensor
182 target site **(Extended Data Fig. 2c, 2d)**.

183 The average editing efficiency among all pegRNAs in the library increased in a time-dependent manner, peaking
184 at ~8% in the final time-point. In general, we observed low indel rates and strong correlation in sensor editing
185 among replicates **(Fig. 1g, Extended Data Fig. 3a-d)**. Strikingly, selecting only the most efficient pegRNA design
186 for each variant led to a two-fold increase in the average editing efficiency, highlighting the utility of the sensor
187 for systematic empirical identification of high efficiency pegRNAs **(Fig. 1g, Extended Data Fig. 3e-g).** Cells with
188 higher editing efficiency also exhibited stronger Nutlin-3 bypass in the Nutlin-3-treatment arm **(Fig. 1g).** Based
189 on the assessment of editing at the sensor locus, we were able to identify active pegRNAs (≥2% editing
190 efficiency) for more than half of the *TP53* variants included in the library. This includes highly efficient pegRNAs
191 that install the desired edit with over 20% efficiency for more than 20% of the variants **(Fig. 1h)**. These pre-
192 validated pegRNAs could be further engineered with silent mutations that evade mismatch repair to boost overall
193 editing efficiency[21].

194 The size and diversity of this library also allowed us to examine features of highly efficient pegRNAs, which
195 broadly recapitulated previous observations[32,33,37,45]. Correlation analysis between various pegRNA features and
196 editing efficiency across all time-points identified the estimated on-target activity of the protospacer (as predicted
197 by Rule Set 2)[46] as the single largest determinant of prime editing efficiency **(Fig. 2a).** In addition, the distance
198 between the edit and the nick introduced by nCas9 was negatively correlated with editing efficiency, while the
199 length of the post-edit homology was positively correlated with editing efficiency **(Fig. 2a).** Thus, edits closer to
200 the nick and with larger post-edit homology were more efficient, consistent with previous findings[32,33,37,45].

201 Notably, the PEGG Score, which is a weighted linear combination of pegRNA features based on literature best
202 practices, correlated more strongly with prime editing efficiency than any other single feature, achieving a
203 Spearman correlation of up to 0.4 **(Fig. 2a-c).** Though this correlation is modest relative to published predictive
204 models[32,33,37], the PEGG score is a simple, unbiased, and cell type/organism-agnostic prediction of pegRNA
205 activity that could complement machine learning-based predictions of PE activity, which may vary due to training
206 on particular cell types.

207 To further analyze the differences in prime editing activity among the 173 protospacers spanning the *TP53* locus,
208 we visualized the number of pegRNAs that utilized each protospacer and the average editing efficiency at each

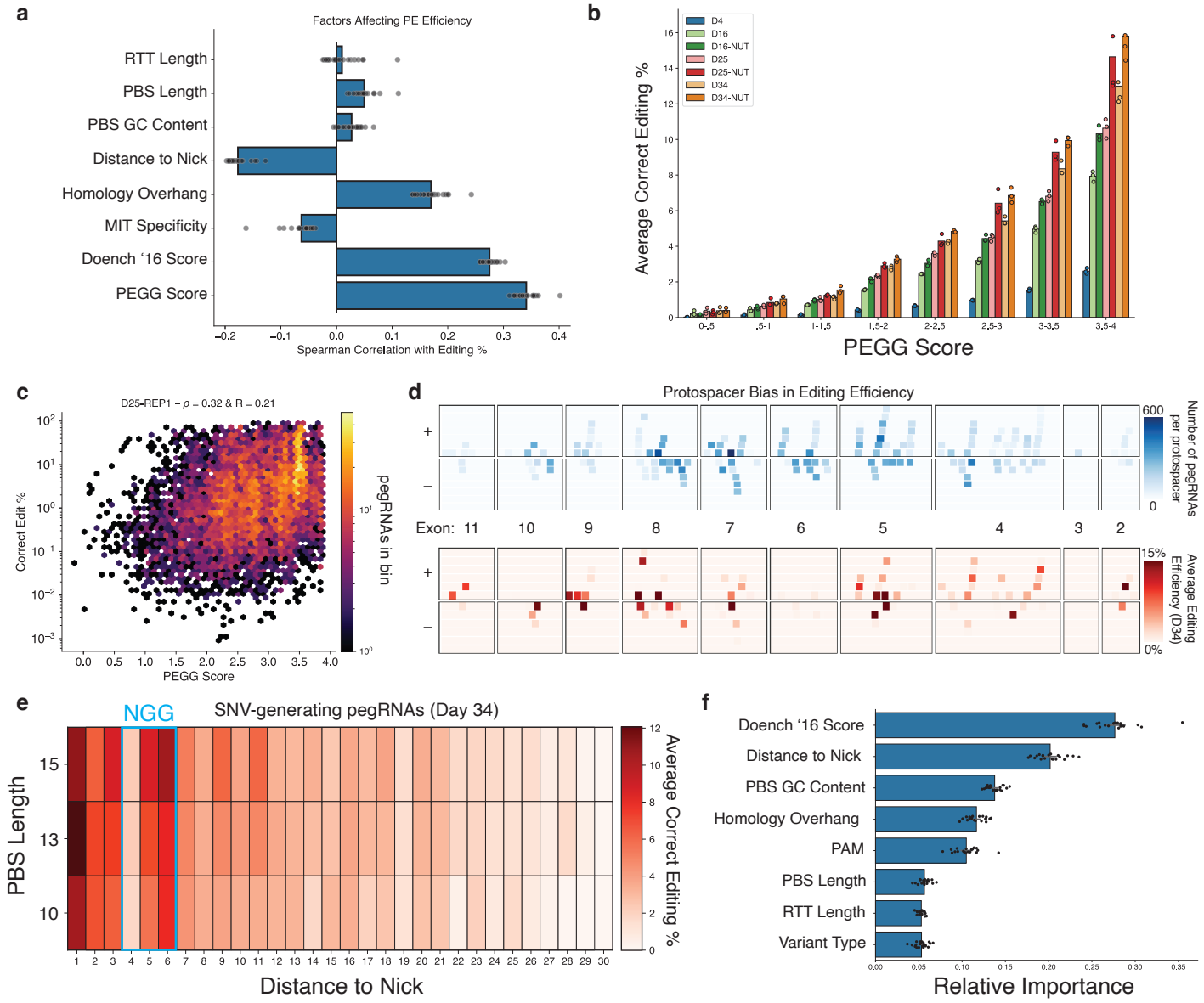

Fig. 2 | Identification of features of highly efficient pegRNAs. a, Spearman correlations between various features of pegRNA design and correct editing percentage, assessed for all pegRNA-sensor pairs with sufficient reads. Each dot represents a separate replicate/time-point. **b,** The relationship between PEGG score and average correct editing percentage at each time-point & condition is monotonically increasing. **c,** A representative example of the correlation between PEGG score and editing efficiency for Day-25 Replicate 1 (Untreated). Spearman correlation = 0.32; Pearson correlation = 0.21. **d,** Visualization of the protospacer bias in editing efficiency. The number of pegRNAs generated per protospacer at each TP53 exon on the plus (+) or minus (-) strand (top) and the average editing efficiency at each of these protospacers at Day 34 of the untreated condition (bottom). **e,** Average editing efficiency for SNV-generating pegRNAs in the library as a function of distance to the nick generated by PEmax and PBS length. The location of the "NGG" PAM sequence is highlighted in blue. Protospacer disrupting (locations +1 to +3) and PAM-disrupting variants (locations +5 & +6) tend to be more efficient. **f,** Feature importances of 20 Random Forest models separately trained to predict pegRNA efficiency. Each dot represents a different model.

209 protospacer **(Fig. 2d)**. This analysis suggests that only a subset of protospacers can be used to generate high
210 efficiency pegRNAs, while other protospacers retain little to no editing activity. We also found that pegRNAs that
211 introduce edits that disrupt the protospacer or PAM sequence tend to be more efficient **(Fig. 2e)**. Relative to the
212 nick created by nCas9, SNVs introduced at the +1–3 position, which mutate the protospacer, and at the +5–6
213 position, which mutate the guanine bases in the NGG PAM, display increased editing activity. In contrast, edits
214 introduced at the +4 position, corresponding to the "N" in the "NGG" PAM sequence, display reduced editing
215 likely due to their failure to disrupt the PAM sequence **(Fig. 2e).**

216 Finally, we trained a random forest regressor to predict pegRNA efficiency **(Extended Data Fig. 4a).** Even with
217 a restricted set of features, this algorithm was able to predict pegRNA activity with a Spearman correlation of
218 ~0.6, comparable to other, more complex algorithms that are used to predict PE activity[32,33,37] **(Extended Data**
219 **Fig. 4b)**. Analysis of the relative feature importances of this random forest model was again consistent with
220 previous findings, and highlighted the GC content of the PBS as another important determinant of editing not
221 identified with simple correlation analysis **(Fig. 2f).** These results demonstrate that large-scale, gene-specific
222 prime editing sensor screening datasets can also provide insight into the determinants of high efficiency prime
223 editing, even though these libraries were not designed with that objective in mind.

224 **Sensor-based calibration of prime editing screening data identifies pathogenic *TP53* variants.**

225 To assess the relative fitness conferred by engineered *TP53* variants, we used the MAGeCK pipeline to
226 normalize read counts among replicates and quantify the $\log_2$ fold-change (LFC) and false discovery rate (FDR)
227 of pegRNAs in the library[47]. While the LFC in pegRNA counts was highly correlated in replicates from the
228 untreated and Nutlin-3-treated arms of the screen, respectively, the correlation among replicates between the
229 two conditions was modest, suggesting that treatment-dependent biological effects were occurring **(Extended**
230 **Data Fig. 3a, 5).** To investigate this further, we used the sensor target site as a quantitative proxy for editing
231 efficiency at the endogenous locus to systematically filter pegRNAs based on their empirical editing efficiency
232 **(Fig. 3a-d, Extended Data Fig. 6a-d)**. As expected, the number of significantly enriched or depleted pegRNAs
233 in "sensor-calibrated" datasets was generally inversely proportional to their editing efficiency, prompting us to
234 focus our statistical analyses on a dataset composed of pegRNAs with ≥10% editing efficiency **(Fig. 3a-e)**. These

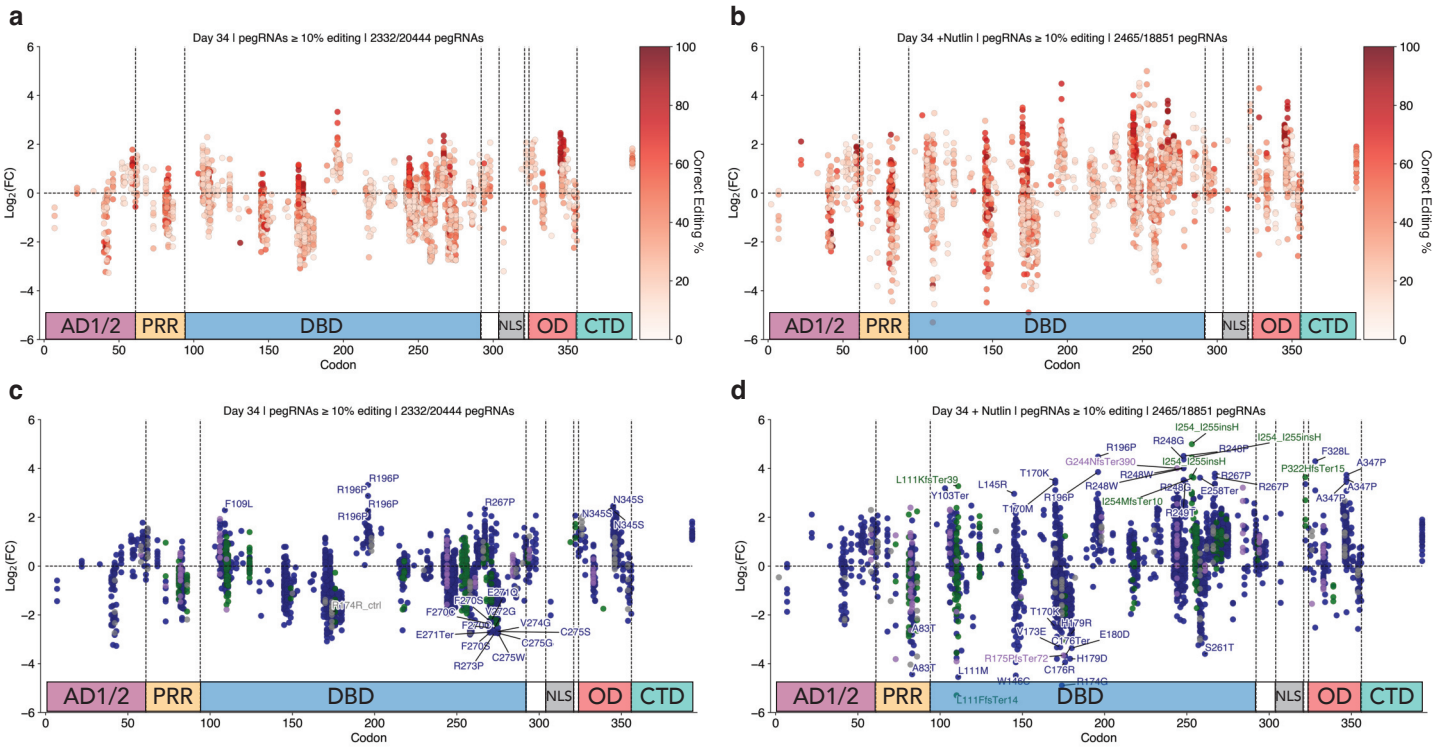

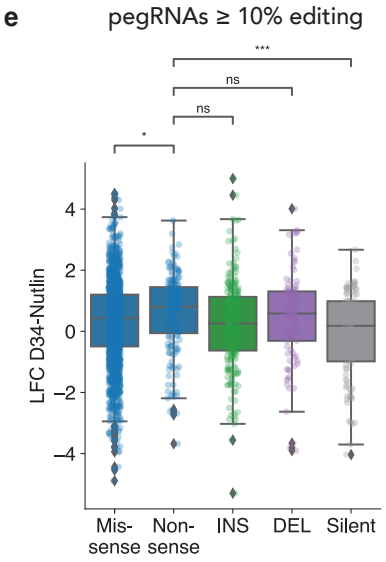

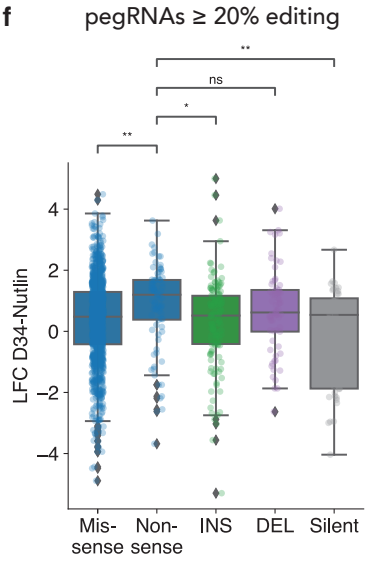

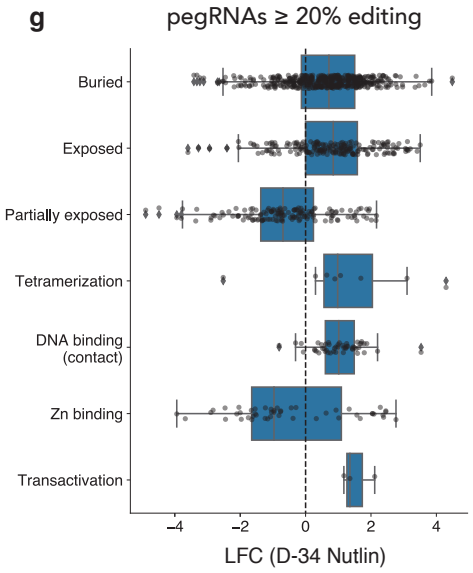

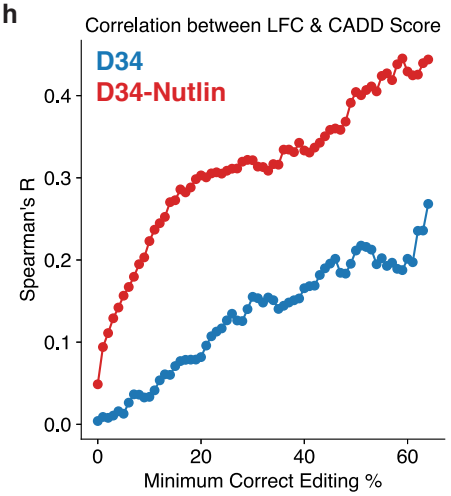

i

peg-8247

Sensor Sequence	Product	HGVSp	% Reads
GCCCCTCCTCAGCATCTTATCCCAGTGGAAGGAAATTTGCGTGTGGAGTATTTGGATGAC	APPQHLIPVEGNLRVEYLDD	R196P	72.90
GCCCCTCCTCAGCATCTTATCCGAGTGGAAGGAAATTTGCGTGTGGAGTATTTGGATGAC	APPQHLIRVEGNLRVEYLDD	WT	9.52
GCCCCTCCTCAGCATCTTATC–GAGTGGAAGGAAATTTGCGTGTGGAGTATTTGGATGAC	APPQHLIEWKEICVWSIWM…	R196EfsTer51	2.13
GCCCCTCCTCAGCATCTTATCCCAGTGGAAGGAAATT-GCGTGTGTGGAGTATTTGGATGAC	APPQHLIPVEGNCVCGVFG*	R196PfsTer13	1.06

peg-5567

Sensor Sequence	Product	HGVSp	% Reads
CTGAGTAGTGGTAATCTACTGGGACCGAACAGCTTTGAGGTGCGTGTTTGTGCCTGTCC	LSSGNLLGPNSFEVRVCAC	R267P	87.35
AATCTACTGGGACGGAACAGCTTTGAGGTGCGTGTTTGTGCCTGTCC	LLGRNSFEVRVCAC	WT_mod	1.73
CTGAGTAGTGGTAATCTACTGGGACGGAACAGCTTTGAGGTGCGTGTTTGTGCCTGTCC	LSSGNLLGRNSFEVRVCAC	WT	1.14

peg-22204

Sensor Sequence	Product	HGVSp	% Reads
ATGGGCGGCATGAACCGGAGGCCCATCCTCACCATCCACATCACACTGGAAGACTCCAGGTC	MGGMNRRPILTIHITLEDSR	I254_I255insH	39.28
ATGGGCGGCATGAACCGGAGGCCCATCCTCACCATCATCACACTGGAAGACTCCAGGTC	MGGMNRRPILTIITLEDSR	WT	36.42

Fig. 3 | High-throughput prime editing sensor screens identify pathogenic *TP53* variants. a, The LFC of each pegRNA ≥ 10% editing with at least 10 sensor reads at Day 34 relative to Day 4 in the untreated condition, with pegRNAs colored by editing efficiency. AD1/2 = activation domain 1/2, PRR = proline rich region, DBD = DNA binding domain, NLS = nuclear localization signal, OD = oligomerization domain, CTD = C-terminal domain. **b,** The LFC of each pegRNA ≥ 10% editing with at least 10 sensor reads at Day 34 relative to Day 4 in the Nutlin-treated condition, with pegRNAs colored by editing efficiency. **c,** Plot (a), but with pegRNAs colored by variant type. Enriching pegRNAs with LFC ≥ 2 and FDR < .05 labeled. Depleting pegRNAs with FDR < .05 labeled. Blue = SNV, Green = INS, Purple = DEL, Gray = Silent. **d,** Plot (b), but with pegRNAs colored by variant type. Selected enriching pegRNAs with FDR < .05 labeled. Depleting pegRNAs with FDR < .05 labeled. Blue = SNV, Green = INS, Purple = DEL, Gray = Silent. **e, f,** Box-plot of LFC in pegRNAs at Day 34 in Nutlin-treated condition separated by variant class for pegRNAs ≥ 10% editing and ≥ 20% editing**.** Statistics shown for t-test of independent samples with Bonferroni correction. * = p-value ≤ .05, ** = p-value ≤ .01, *** = p-value ≤ .001, **** = p-value ≤ .0001, ns = not significant (p-value > .05). **g,** Box-plot of the LFC at Day 34 in the Nutlin-treated condition for pegRNAs ≥ 20% editing with annotated residue functions. **h,** Spearman correlation between LFC of SNV-generating variants and CADD score at Day 34 in untreated (blue) and Nutlin-treated (red) conditions at minimum correct editing thresholds spanning 0% to 65%. **i,** Sensor editing for selected pegRNAs at Day 34 in the Nutlin-treated condition.

235 results demonstrate that our sensor-based approach allows empirical removal of pegRNAs that exhibit potentially
236 spurious enrichment or depletion, and low and/or undesired editing activity, retaining pegRNAs that are
237 significantly more likely to introduce the variants of interest.

238 As hypothesized, the dynamic range in the Nutlin-3-treated arm of the screen was significantly higher than the
239 untreated arm, with pegRNAs more strongly enriching and depleting in the presence of Nutlin-3 **(Fig. 3a, 3b).**
240 Treatment with Nutlin-3 also selected for cells with higher efficiency editing, improving the resolution of the screen
241 **(Fig. 3a, 3b)**. Several putative pathogenic *TP53* variants, including R196P and R267P, were strongly enriched
242 in both treatment arms, with multiple pegRNAs per variant appearing as top hits **(Fig. 3c, 3d).** Given the higher
243 dynamic range of the Nutlin-3 treatment arm, as well as the possibility that this treatment biases towards the
244 discovery of dominant negative *TP53* mutations[2,6,16], we focused our analyses on this treatment group. Multiple
245 *TP53* variants showed significant enrichment in the Nutlin-3-treatment group, including SNVs and indels in the
246 C-terminal half of the DNA-binding domain (DBD) and the oligomerization domain (OD) **(Fig. 3d)**. This includes
247 multiple variants at residues 248 and 249, which are known mutational hotspots in p53 and commonly observed
248 in cancer patients and individuals with the Li-Fraumeni cancer predisposition syndrome[17].

249 Provocatively, the most commonly observed *TP53* mutation, R175H, did not show strong enrichment despite the
250 existence of multiple R175H pegRNAs exhibiting ≥10% editing efficiency. In fact, the majority of the top enriching
251 variants we identified were not in known mutational hotspots[19], suggesting that other types of variants can
252 produce stronger phenotypes. These include the top hit, an insertion of a histidine between residues 254 and
253 255, as well as R196P and multiple variants in the oligomerization domain (F328L, N345S, A347P) **(Fig. 3d).**
254 These observations are consistent with the possibility that some *TP53* hotspot mutations are observed in part
255 due to disproportionately high mutagenesis rates at the genomic level due to extrinsic and intrinsic factors, such
256 as tobacco smoke and APOBEC activity, rather than only due to the fitness advantage conferred by these
257 variants relative to other *TP53* mutations[6,19]. We also identified strongly depleting variants in the DBD that may
258 retain wild type p53 transcriptional activity or fail to exert a dominant negative effect on the p53 tetramer **(Fig.**
259 **3d).** Collectively, these results validate the utility of our approach and dataset to accurately identify pathogenic
260 *TP53* variants.

261 Bulk quantification of pegRNAs grouped by variant class also revealed that nonsense variants were significantly
262 more enriched compared to missense and silent variants. This is evident at multiple thresholds of pegRNA
263 activity **(Fig. 3e, 3f).** As expected, silent variants tend to deplete, particularly when considering pegRNAs at
264 higher threshold for editing efficiency (≥ 20%), bolstering our confidence in the fidelity of the screen **(Fig. 3f).**
265 Using available annotations of p53 residue function[48], we also found that, as expected, variants in DNA
266 binding/contacting residues displayed strong enrichment (including residues 248 and 273) **(Fig. 3g)**. Intriguingly,
267 certain variants involved in tetramerization and transactivation (e.g., L22V) were also strongly enriched, despite
268 the low frequency of mutation in these residues **(Fig. 3g)**. Other observations are more difficult to interpret, such
269 as the large variance in the enrichment of mutations that affect residues involved in zinc binding, or the fact that
270 variants in partially exposed residues tended to deplete while those in buried and exposed residues tended to
271 enrich **(Fig. 3g).** Altogether, these observations suggest that there is a large, underappreciated phenotypic
272 variance in the relative fitness conferred by distinct *TP53* variants — not all p53 variants are one and the same,
273 a concept that is likely relevant across many other genes and more broadly in biology.

274 We also sought to quantify the degree of concordance between our screening results and widely used metrics
275 of variant deleteriousness. To do so, we used the Combined Annotation-Dependent Depletion (CADD) score,
276 which integrates evolutionary conservation of residues with other metrics of pathogenicity to generate a CADD
277 score, with higher scoring variants predicted to be more deleterious[49]. We observed a low correlation between
278 CADD score and enrichment of all SNV-specific pegRNAs. However, the correlation between CADD score and
279 variant-specific fitness increased dramatically when we used sensor target sites to restrict our analysis to variants
280 generated by high efficiency pegRNAs **(Fig. 3h)**. We achieved a Spearman correlation of ~0.3 when considering
281 Nutlin-3-treated pegRNAs with ≥ 15% editing activity, and >0.4 when considering pegRNAs ≥ 50% editing **(Fig.**
282 **3h)**. Across all minimum pegRNA editing activity thresholds, the CADD score correlated more strongly with
283 fitness of Nutlin-3-treated pegRNAs to the untreated condition. These results emphasize the significant
284 advantage of including sensor target sites in prime editing screening libraries to assess pegRNA efficiency and
285 reinforce the ability of Nutlin-3 to effectively pull out genuine LOF, GOF, and separation-of-function *TP53* variants
286 **(Fig. 3h, 3i).**

287 **Sequencing of endogenous *TP53* validates the prime editing sensor approach**

288 The above results demonstrate that sensor-calibrated quantification of pegRNA enrichment and depletion can
289 be used to identify *bona fide* pathogenic *TP53* variants. However, these analyses do not rule out the possibility
290 that these changes are independent of true editing at the endogenous *TP53* locus. To formally test if prime
291 editing sensor screens can faithfully quantify the effects of variants engineered at endogenous loci, we performed
292 targeted next-generation sequencing of specific regions in exons 6, 7, and 10 of *TP53* using genomic DNA
293 extracted from untreated and Nutlin-treated cells from Day 4 and Day 34 timepoints **(Fig. 4a)**. We reasoned that
294 sequencing the native *TP53* locus would allow us to directly compare the fold-change in pegRNA counts with
295 the fold-change of variants installed at defined targeted sites within endogenous *TP53*.

296 Unlike non-sensor-based prime editing screens, which are likely to suffer from significant noise during
297 enrichment due to the difficulty of designing high efficiency pegRNAs, our sensor-based prime editing screen
298 could be empirically denoised by filtering for pegRNAs that edited their cognate sensor above a given editing
299 threshold. Indeed, we observed no correlation between the LFC in pegRNA counts with the corresponding LFC
300 of endogenous variants engineered in the native *TP53* locus when considering all pegRNAs **(Fig. 4b-d)**.
301 However, taking advantage of the sensor site to filter out pegRNAs below a given correct editing threshold
302 dramatically reduced the noise in this data and revealed a strong correlation between the fold-change in pegRNA
303 counts and endogenous variant counts **(Fig. 4b, 4c)**. This correlation increased monotonically as the minimum
304 correct editing threshold increased, reaching a Spearman correlation > 0.4 in the untreated arm and > 0.5 in the
305 Nutlin-treated arm of the screen when using a minimum correct editing threshold of 50% **(Fig. 4d)**. Moreover,
306 edited exonic sites targeted by top enriching pegRNAs (e.g. R196P, A347P, I254_I255insH) were significantly
307 enriched relative to their wild type counterparts and strongly correlated with their respective pegRNA counts. In
308 addition, we were able to detect nearly all of the variants engineered by active pegRNAs (≥ 500 counts per
309 variant and ≥ 1% correct sensor editing), and the detectable fraction reached saturation when considering
310 pegRNAs producing ≥ 14% editing at the sensor site **(Fig. 4e)**. Altogether, these results emphasize the
311 essentiality of integrating quantitative, sensor-like approaches to accurately extract true signal from the high
312 levels of noise that are inherent in large-scale prime editing screens. Indeed, our analysis demonstrates that

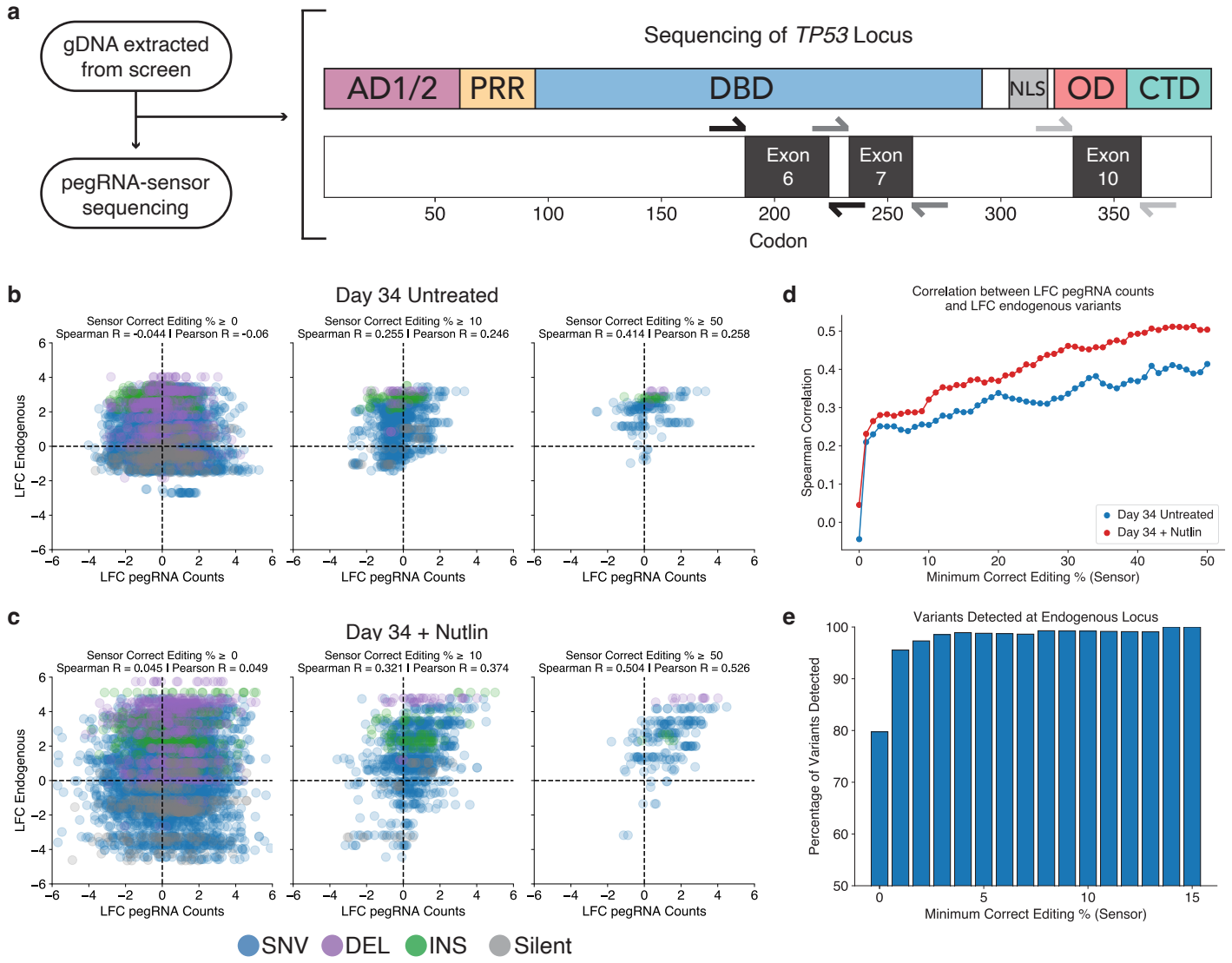

Fig. 4 | Sequencing of TP53 validates the prime editing sensor approach. a, Schematic of the sequencing of the TP53 locus. Regions within exons 6, 7, and 10 were sequenced from genomic DNA extracted at Day 4 and Day 34 in the untreated and Nutlin-treated arm of the screen. **b,** Correlation between the LFC in pegRNA counts and the LFC of endogenous variants at the TP53 locus for Day 34 vs. Day 4 of the untreated arm of the screen at different thresholds of pegRNA editing activity. **c,** Correlation between the LFC in pegRNA counts and the LFC of endogenous variants at the TP53 locus for Day 34 vs. Day 4 of the Nutlin-treated arm of the screen at different thresholds of pegRNA editing activity. **d,** Spearman correlation between the LFC in pegRNA counts and the LFC of endogenous variants at the TP53 locus as a function of the minimum sensor correct editing threshold for Day 34 untreated (blue) and D34 Nutlin-treated (red) samples. **e,** The percentage of variants detected (≥ 500 counts) at the TP53 locus at Day 34 (untreated) for variants with pegRNAs at different minimum sensor correct editing thresholds.

313 screening pegRNAs without any empirical quantification of their editing activity invariably leads to spurious
314 conclusions concerning the fitness of the variants that those pegRNAs are intended to engineer.

315 **Functional validation of pathogenic *TP53* variants identified with prime editing screening**

316 The above data demonstrate that pegRNA-specific sensor modules can be used to rigorously calibrate screening
317 results to limit the analysis of variant fitness effects only to highly efficient pegRNAs. Though suggestive, these
318 results do not formally prove that top scoring pegRNAs are enriched due to the introduction of defined genetic
319 variants at the endogenous target locus and that these drive the observed biological differences. To test this, we
320 selected a cohort of 29 pegRNAs that significantly enriched or depleted in the screen, or that generated
321 commonly observed "hotspot" mutations **(Fig. 5a, 5b)**. This set of pegRNAs targeted residues that spanned the
322 *TP53* locus and also included two control pegRNAs that install silent edits **(Fig. 5a, 5b)**. In all, this validation set
323 included low, medium, and high efficiency pegRNAs spanning a range of 0 to 86% correct editing percentages,
324 as measured by their respective sensor sites **(Fig. 5c)**. We transduced A549-PEmax cells with lentiviruses
325 encoding individual pegRNAs and allowed editing to occur for 7–10 days, based on the kinetics of editing we
326 observed previously **(Fig. 1f)**. We then mixed each individual population of sequence-verified isogenic A549-
327 PEmax-pegRNA cells with parental *TP53* wild type A549-PEmax cells and performed longitudinal fluorescence
328 competition assays in the presence or absence of Nutlin-3 **(Fig. 5d, Extended Data Fig. 7)**. We used the RFP
329 fluorophore linked to each pegRNA vector to track the relative fitness of pegRNA cells (RFP+) compared to
330 parental cells (RFP-) **(Fig. 5d).** These competition assays proceeded for two weeks, with flow cytometry readings
331 taken every 7 days for each replicate **(Fig. 5d, Extended Data Fig. 8)**. We then calculated the difference in the
332 RFP+ cell fraction (ΔRFP+ %) for each pegRNA between the final and initial time-point in both conditions **(Fig.
333 5e).** Consistent with our screening results, a significant fraction of pegRNAs showed enrichment in the presence
334 of Nutlin-3, often reaching complete saturation **(Fig. 5e)**. Overall, there was strong concordance between the
335 enrichment in Nutlin-3-treated cells observed in the screen and in these competition assays, supporting the
336 reproducibility of the screening results **(Fig. 5f).** Importantly, we observed a significantly strong enrichment of
337 cells expressing pegRNAs designed to engineer variants in the oligomerization domain, including A347P **(Fig.
338 5d, 5f).**

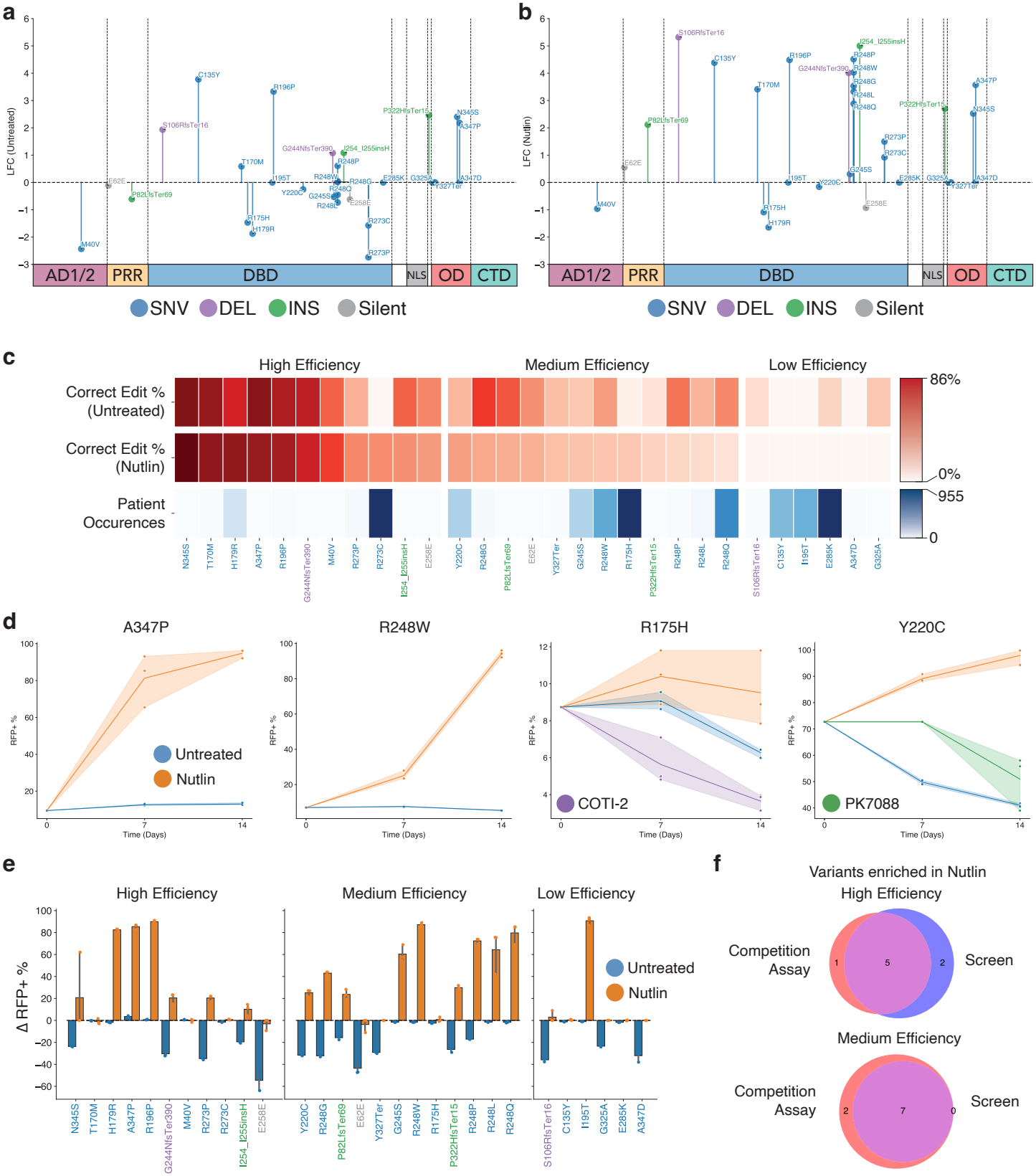
a
LFC (Untreated)
AD1/2
PRR
DBD
NLS
OD
CTD
SNV
DEL
INS
Silent
b
LFC (Nutlin)
c
High Efficiency
Medium Efficiency
Low Efficiency
Correct Edit % (Untreated)
Correct Edit % (Nutlin)
Patient Occurences
86%
0%
955
0
d
A347P
R248W
R175H
Y220C
RFP+ %
Time (Days)
Untreated
Nutlin
COTI-2
PK7088
e
High Efficiency
Medium Efficiency
Low Efficiency
Δ RFP+ %
Untreated
Nutlin
f
Variants enriched in Nutlin
High Efficiency
Competition Assay
Screen
Medium Efficiency
Competition Assay
Screen

Fig. 5 | Functional validation of pathogenic *TP53* variants identified with prime editing screening. a, LFC of 29 pegRNAs selected for validation at Day 34 in the untreated condition. Variants with insufficient control counts (I195T, E285K, G325A, Y327Ter, A347D) represented with LFC = 0. **b,** LFC of 29 pegRNAs selected for validation at Day 34 in the Nutlin-treated condition. Variants with insufficient control counts (I195T, E285K, G325A, Y327Ter, A347D) represented with LFC = 0. **c,** Visualization of correct editing percentages and number of patient occurrences (MSK-IMPACT) for the pegRNAs selected for validation. **d,** Selected competition assays show the change in the RFP positive cell fraction in the presence or absence of various selection agents. **e,** The change in the RFP positive cell fraction (ΔRFP+ %) at the initial versus final time-point for each variant in the presence or absence of Nutlin-3. **f,** Venn diagram visualizing the agreement between enrichment in the presence of Nutlin in the competition assays (ΔRFP+ % ≥ 5) and the original screen (LFC ≥ 1) for high and medium efficiency pegRNA validation sets.

339 The above results indicate that cells harboring a number of pegRNAs designed to engineer diverse types of
340 *TP53* variants have an increased fitness. However, these results do not rule out the possibility that these
341 pegRNAs confer increased fitness through indel generation, rather than through their encoded edits. To assess
342 this, we performed targeted Sanger sequencing and NGS across each of the target loci in A549-PEmax-pegRNA
343 cells. Consistent with our screening data, sensor measurements, and competition assay results, each edited cell
344 line exhibited specified on-target prime editing, in some instances reaching apparent homozygosity **(Extended**
345 **Data Fig. 7)**.

346 Another potential application of our approach is to combine high-throughput prime editing with drug treatments
347 to identify variant-drug interactions that could be exploited to develop allele-specific therapies. This is particularly
348 relevant today because recent advances in rational drug design have shown that small molecules targeting
349 specific mutant proteins (including those produced by oncogenic point mutant *KRAS* alleles) can have significant
350 therapeutic potential[50]. To test if our approach could be used to identify variant-specific therapeutic sensitivities,
351 we tested two mutant-p53-specific therapeutic agents, COTI-2 and PK7088, in cells transduced with lentiviruses
352 encoding R175H- and Y220C-targeting pegRNAs, respectively[51–53]. Both of these treated populations showed
353 depletion in the RFP+ cell fraction **(Fig. 5d).** In particular, the COTI-2 treatment arm showed significant depletion
354 of R175H-pegRNA cells **(Fig. 5d).** These results demonstrate that prime editing sensor screens could be used
355 to systematically identify variant-specific vulnerabilities to diverse therapies, augmenting cDNA-based
356 approaches for performing similar screens[54].

357 **Comparative analysis of prime editing and cDNA screening datasets reveals new pathogenic variants in**
358 **the p53 oligomerization domain**

359 High-throughput functional genomics approaches have been used previously to investigate *TP53* mutations. For
360 instance, Giacomelli et al. performed deep mutational scanning of *TP53* variants using exogenous
361 overexpression of mutant *TP53* cDNAs in A549 cells in the presence or absence of Nutlin-3, concluding that
362 most *TP53* mutations likely arise as a consequence of endogenous mutational processes that select for dominant
363 negative and LOF activity[6]. A follow up study integrated this method with HDR-based modeling of six *TP53*
364 hotspot mutations in human leukemia cells and concluded that missense mutations in the *TP53* DBD act solely

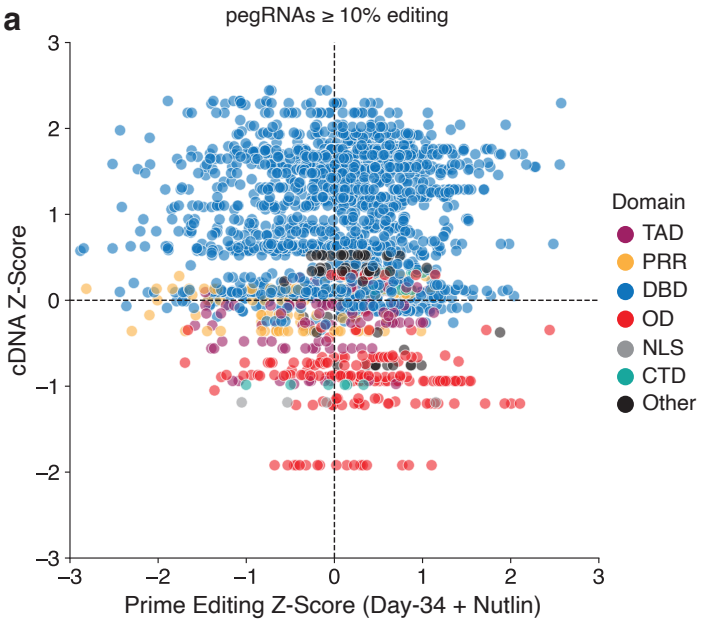
a
pegRNAs ≥ 10% editing
cDNA Z-Score
Prime Editing Z-Score (Day-34 + Nutlin)
Domain
TAD
PRR
DBD
OD
NLS
CTD
Other

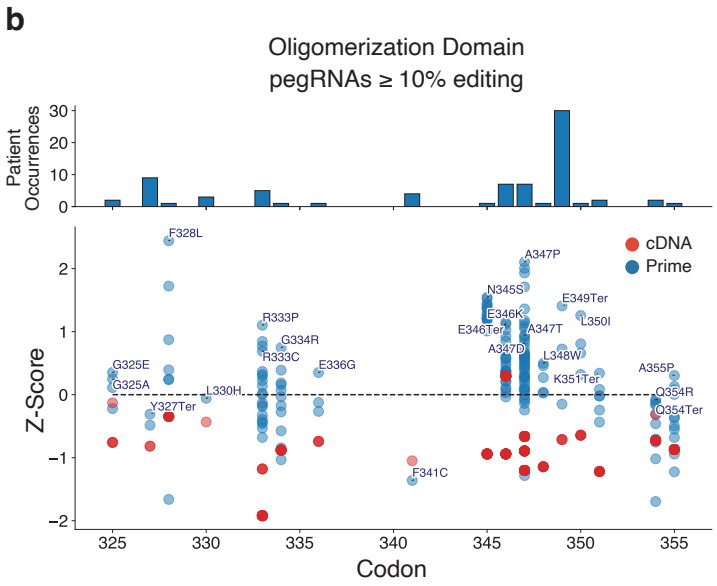
b
Oligomerization Domain
pegRNAs ≥ 10% editing
Patient Occurrences
Z-Score
Codon
cDNA
Prime
F328L
A347P
N345S
E349Ter
E346K
E346Ter
A347T
L350I
A347D
L348W
K351Ter
A355P
Q354R
Q354Ter
R333P
G334R
R333C
E336G
G325E
G325A
L330H
Y327Ter
F341C

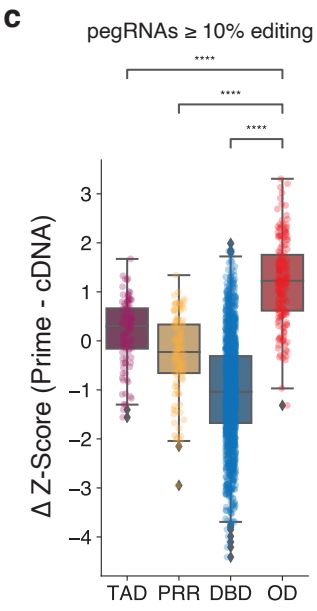
c
pegRNAs ≥ 10% editing
Δ Z-Score (Prime - cDNA)
TAD
PRR
DBD
OD

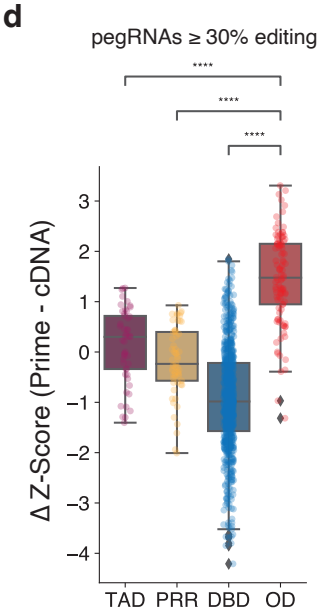
d
pegRNAs ≥ 30% editing
Δ Z-Score (Prime - cDNA)
TAD
PRR
DBD
OD

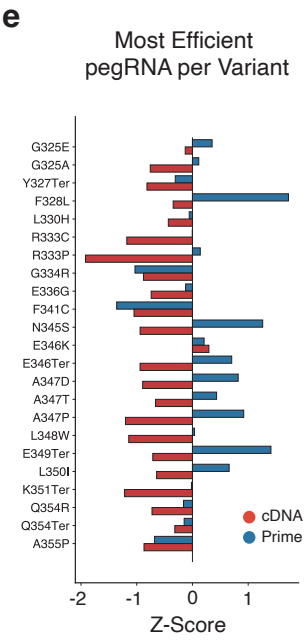
e
Most Efficient pegRNA per Variant
G325E
G325A
Y327Ter
F328L
L330H
R333C
R333P
G334R
E336G
F341C
N345S
E346K
E346Ter
A347D
A347T
A347P
L348W
E349Ter
L350I
K351Ter
Q354R
Q354Ter
A355P
cDNA
Prime
Z-Score

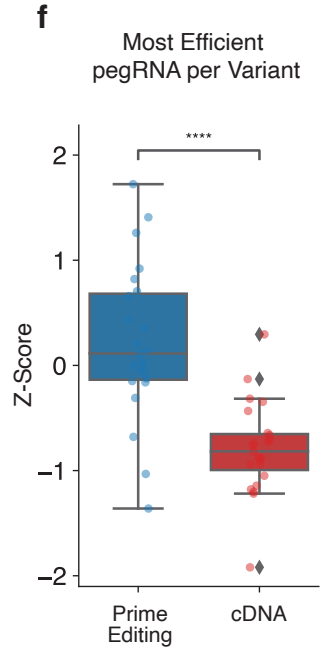
f
Most Efficient pegRNA per Variant
Z-Score
Prime Editing
cDNA

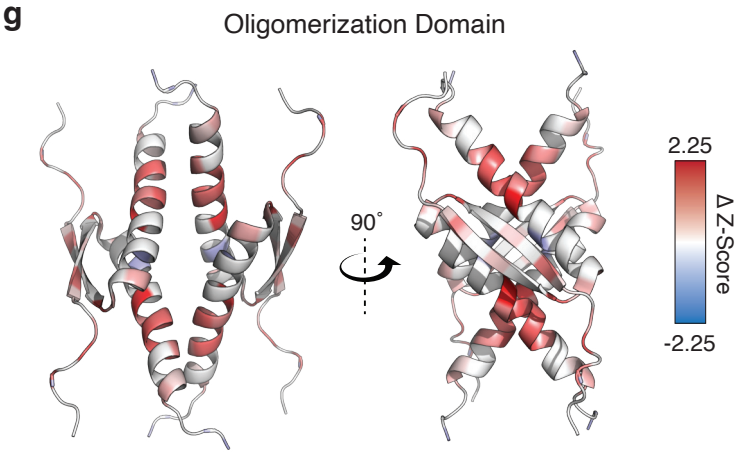
g
Oligomerization Domain
90°
2.25
Δ Z-Score
-2.25

Fig. 6 | Comparative analysis of prime editing and cDNA screening datasets of *TP53* variants reveals novel pathogenic variants in the oligomerization domain. a, Scatter-plot of prime editing Z-score for pegRNAs ≥ 10% editing at Day 34 in the Nutlin-treated condition, and the corresponding cDNA variant Z-score in the p53-WT background in the presence of Nutlin, colored by p53 domain. **b,** cDNA (red) and prime editing (blue) Z-scores for pegRNAs/variants located in the oligomerization domain. The pegRNA with the highest Z-score is labeled. **c, d,** The difference in Z-scores between prime editing and cDNA screens (ΔZ-score) for pegRNAs ≥ 10% and ≥ 30% editing, separated by p53 domain. Statistics shown for t-test of independent samples with Bonferroni correction. * = p-value ≤ .05, ** = p-value ≤ .01, *** = p-value ≤ .001, **** = p-value ≤ .0001, ns = not significant (p-value > .05). **e,** Z-scores for variants in the cDNA (red) and prime editing (blue) screens, considering only the most efficient pegRNA for each variant with an editing efficiency ≥ 10%. **f,** Box-plot of the z-scores for variants in the cDNA (red) and prime editing (blue) screens, considering only the most efficient pegRNA for each variant. Statistics shown for t-test of independent samples with Bonferroni correction; **** = p-value ≤ .0001. **g,** Visualization of the residue-averaged ΔZ-scores (pegRNAs ≥ 10% editing) on an NMR-structure of p53 oligomerization domain (PDB: 1OLG).

365 through dominant negative activity[2]. More recently, Ursu et al. employed a modified version of Perturb-seq to
366 interrogate the transcriptional effects of 200 mutant *TP53* cDNAs in A549 cells by single cell RNA-sequencing,
367 also concluding that most of these disrupt p53 activity through LOF and dominant negative effects[16]. In contrast,
368 another study used a similar approach in H1299 and HCT116 cell lines to interrogate variants in the *TP53* DBD
369 through parallel *in vitro* and *in vivo* experiments, concluding that certain hotspot mutations confer a higher
370 proliferative advantage *in vivo*, likely through GOF mechanisms[7]. A number of studies in both mice and humans
371 have also demonstrated that certain *TP53* variants, including hotspot mutations at residues R175, R248, and
372 R273, can produce phenotypes consistent with neomorphic/GOF activities[55]. These include promoting aberrant
373 self-renewal of hematopoietic stem cells[56], sustaining tumor growth[57,58], and promoting metastatic
374 dissemination[59–62], among others[55]. As such, there is much controversy in the field regarding the precise cellular
375 and molecular activities of cancer-associated *TP53* mutations — the most common genetic lesions observed
376 across all types of cancer.

377 We hypothesized that cDNA screening approaches are biased in favor of detecting dominant negative activities
378 due to their reliance on supraphysiological overexpression of mutant proteins. This is particularly relevant for
379 studying the active p53 transcription factor, which is a tetrameric protein composed of a dimer of dimers[18]. As
380 such, we postulated that mutant overexpression studies in wild type *TP53* cells, including A549, may be
381 incapable of detecting mutant allele-specific activities and phenotypes that may be sensitive to gene dosage and
382 protein stoichiometry. To test this hypothesis, we reanalyzed our data to perform comparative bioinformatic
383 analyses with the dataset generated by Giacomelli et al.[6], as their experiments were also carried out in wild type
384 *TP53* A549 cells treated with Nutlin-3. First, we plotted the Z-scores of SNV-generating pegRNAs (≥10% editing)
385 against the Z-scores of the corresponding variants expressed from cDNAs **(Fig. 6a).** Supporting our hypothesis,
386 variants in the OD of p53 tended to deplete (i.e., Z-score<0) when expressed from cDNAs, but often enriched
387 significantly when expressed from the endogenous locus **(Fig. 6a, 6b)**. To investigate this difference further, we
388 calculated the difference in Z-scores (ΔZ-score) between each pegRNA–cDNA pair by subtracting the prime
389 editing Z-score from the cDNA Z-score. This analysis revealed a significantly higher ΔZ-score for endogenous
390 variants in the OD relative to other domains of p53 **(Fig. 6c, 6d**), a pattern that consistently held at multiple
391 thresholds of pegRNA activity, and even when we restricted our analysis solely to the most efficient pegRNA for

392 each variant **(Fig. 6e, 6f).** Some of the most impactful variants in the p53 OD are frequently observed in
393 individuals with Li-Fraumeni syndrome, who carry germline *TP53* variants that predispose them to cancer.
394 Importantly, recent studies by the Prives and Lozano laboratories have shown that p53 proteins harboring A347D
395 mutations (in the OD) form stable dimers instead of tetramers, and that these dimeric p53 proteins exhibit
396 neomorphic activities[63,64]. Lastly, visualizing the residue-averaged ΔZ-scores on the structure of the p53 OD[65]
397 further highlights the extensive differences in the behavior of endogenous variants as compared to exogenous
398 (cDNA) variants in this domain **(Fig. 6g).** Collectively, our observations highlight gene dosage, protein
399 stoichiometry, and protein-protein interaction domains as important variables that must be taken into account
400 when studying the enormous diversity of mutant alleles observed in human cancer. Failing to take these
401 considerations into account might lead to the misclassification of *bona fide* pathogenic variants, including those
402 identified in patients with hereditary cancer predisposition syndromes like Li-Fraumeni.

403 **Discussion**

404 The overwhelming majority of genetic variants associated with various human diseases, including cancer, remain
405 uncharacterized[40]. The development of CRISPR-based precision genome editing tools, including base and prime
406 editing[9,10], has opened the door to rigorous experimental interrogation of disease-associated variants with single
407 base-pair resolution at unprecedented scales. However, these approaches, particularly prime editing, remain
408 limited by the variance in editing efficiency among different pegRNAs.

409 Building on our previous work, we developed a new prime editing sensor-based framework for engineering and
410 screening variants that overcomes these limitations. Using this sensor-based approach, in which each pegRNA
411 is coupled to an artificial version of its endogenous target site, we simultaneously identify enriched pegRNAs
412 while empirically quantifying their editing efficiencies. This novel approach allows for the characterization of
413 variants at multiple target sites while correcting for the potentially confounding differences in editing activity
414 among distinct pegRNAs. To facilitate the creation of similar libraries by other researchers, we also built PEGG,
415 a new computational tool for creating prime editing sensor libraries (pegg.readthedocs.io).

416 As a prototype for the prime editing sensor framework, we generated a library of pegRNAs targeting over a
417 thousand cancer-associated variants in *TP53*. We reasoned that p53 would be the most salient prototype for
418 testing the efficacy of our prime editing sensor screening platform because of its central role in cancer
419 development and progression, the various studies that have performed deep mutational scanning of p53 whose
420 data can provide direct sources of comparison, and the ongoing controversy in the field as to whether most (if
421 not all) *TP53* mutations observed in cancer patients are functionally redundant.

422 With our sensor-based approach, we were able to systematically search the pegRNA design space and identify
423 high efficiency pegRNAs, allowing us to install over half of the targeted *TP53* variants. Though not the focus of
424 the present study, this dataset also allowed us to recapitulate many of the previous findings about the factors
425 affecting pegRNA efficiency.

426 Analysis of the screening data revealed a wide range in the fitness of *TP53* variants, challenging the idea that
427 most p53 variants, particularly those in the DBD, are functionally redundant. We identified strongly enriching
428 pegRNAs, including pegRNAs that generated "hotspot" mutations that are commonly observed in patients,
429 particularly those at DNA-contacting residues. However, the majority of the strongly enriching pegRNAs encoded
430 variants that are not located at mutational hotspots; instead, a number of these mutations are less frequently
431 observed in patients and remain poorly understood, despite the fact that they affect thousands of patients globally
432 every year. These include variants located within the OD of p53, which were functionally validated with follow-
433 up experiments and some of which were recently shown to be *bona fide* pathogenic variants in humans with Li-
434 Fraumeni Syndrome[63,64].

435 Comparison between our screening data and a previous study that also screened *TP53* variants in A549 cells
436 and in the presence of Nutlin-3 but instead used cDNA-based overexpression libraries revealed a statistically
437 significant enrichment of endogenous — but not overexpressed — variants located in the p53 OD. This
438 comparison highlights the potential limitations of cDNA-based screening approaches, particularly when studying
439 variants at the sites of protein-protein interactions, underscoring the need to study variants in their native context
440 to access their true biology. Together, our data suggest that stoichiometric imbalances produced by cDNA
441 overexpression could lead to the mis-classification of genetic variants as non-causal or otherwise benign. Our

442 findings thus offer a cautionary note when using exogenous overexpression systems to interpret pathogenic
443 alleles, and highlight the importance of using strategies like the one described in this work to investigate variants
444 of interest in their native genomic contexts whenever possible.

445 More broadly, our study provides a conceptual blueprint and a modular set of experimental and computational
446 tools that can be applied to evaluate diverse types of genetic variants in their native endogenous genomic
447 contexts with high-throughput prime editing. Future efforts could incorporate improved prime editors and
448 pegRNAs, as well as higher-efficiency prime editing systems such as PE3 and PE4[10,21]. These studies could
449 also be performed *in vivo*, for example by delivering compact libraries of MMR-evasive pegRNAs into mice
450 expressing prime editors[66] or by co-delivery of smaller prime editors, such as PE6a[23]. Taken together, we
451 envision that our approach will expand our understanding of pathogenic gene variants and help match patients
452 suffering from genetic diseases with effective therapies.

453 **Methods**

454 **Experimental Materials & Methods:**

455 **Plasmids and pegRNA cloning.** All plasmids were generated using Gibson Assembly strategies[67] using
456 NEBuilder® HiFi DNA Assembly Master Mix (NEB #E2621) following the manufacturer's protocol. All new
457 plasmids, along with detailed maps and sequences, will be made available through Addgene. The PEmax coding
458 sequence in Lenti-EFS-PEmax-P2A-Puro was obtained from pCMV-PEmax (Addgene, catalog no. 174820)[21].
459 The lentiviral plasmid used to clone and express prime editing sensor libraries was assembled by transferring
460 the U6-sgRNA-EFS-Blast-P2A-TurboRFP cassette from pUSEBR[14] into the higher titer pLV backbone[68]. Lenti-
461 PEAR-mCherry, a modified all-in-one lentiviral version of the PEAR[43] reporter, was also cloned using Gibson
462 Assembly and used to test the editing activity of A549-PEmax cells. The Lenti-UPEmS-tevo plasmid is a modified
463 version of the UPEmS vector[66] that contains the tevopreQ1 motif[22]. This plasmid was used to assemble pegRNAs
464 via Golden Gate Assembly[66] for follow-up pegRNA validation experiments.

465 **Virus Production:**

466 Lentiviruses were produced by co-transfection of HEK293T cells with the relevant lentiviral transfer vector and
467 packaging vectors psPAX2 (Addgene, catalog no. 12260) and pMD2.G (Addgene, catalog no. 12259) using
468 Lipofectamine 2000 (Invitrogen, catalog no. 11668030). Viral supernatants were collected at 48- and 72-hours
469 post-transfection and stored at -80°C.

470 **Drug treatments:**

471 Nutlin-3 (Selleck Chemicals, S1061) was dissolved in DMSO at a stock concentration of 10 mM and used at a
472 final concentration of 10 μM. PK7088 (Aobious #AOB4255) was diluted to a final concentration of 200 μM from
473 a stock concentration of 10 mM. COTI-2 (MedChemExpress #HY-19896) was dissolved in DMSO to a stock
474 concentration of 10 mM and added to a final concentration of 1 μM.

475 **Flow Cytometric Analyses:**

476 Fluorescence-based measurements for the validation of prime editing activity with PEAR and for competition
477 assays were performed using the BD FACSCelesta Cell Analyzer in tube or plate reader format. Downstream
478 analysis was performed using FlowJo to identify single cells and quantify fluorescence.

479 **Generation of A549-PE Max cell lines:**

480 To generate A549 cells stably expressing PEmax, we transduced a 15-cm plate with 2.5 million cells with freshly
481 harvested EFS-PEmax-P2A-Puromycin lentivirus, and selected cells with 10 μg/mL of puromycin at 72-hours
482 post-transduction. To assess the prime editing efficiency of these cells, we transduced 250K A549-PEmax cells
483 in triplicate in 6-well plates with Lenti-PEAR-mCherry, a modified, all-in-one lentiviral PEAR construct, where
484 GFP is turned on in the event of successful prime editing. We noticed that prime editing activity was not
485 sufficiently high in these cells based on the PEAR reporter activity. We then re-transduced these cells with 2
486 successive rounds of freshly harvested EFS-PEmax-P2A-Puromycin lentivirus. Repeating the PEAR reporter
487 assay revealed a substantial increase in prime editing activity **(Extended Data Fig. 2a)**. This A549-PEmax "v2"
488 cell line was used throughout the present study.

489 **Cloning of p53-sensor Library:**

490 The oligonucleotide library was ordered from Twist Biosciences. The lyophilized library was resuspended in 100
491 µL of TE Buffer (pH 8.0) and diluted to create 1 ng/µL stocks. We performed n=32 PCR reactions with NEBNext
492 High-Fidelity 2X PCR Master Mix (#M0541S) to amplify the library with the following primers at a low cycle count:
493 (1) F: 5′-CATAGCGTACACGTCTCACACCG, (2) R: 5′-GTGCCGTTGACGACCGGATCTAGAATTC. These PCR
494 reactions were pooled and PCR purified using the Qiagen PCR purification kit following the manufacturer's
495 protocols, with 10 µL of 3 M NaOAc pH 5.2 added for every 5 volumes of PB used per 1 volume of PCR reaction.
496 The library was digested with Esp3I (NEB) and EcoRI-HF (NEB), pooled and PCR purified. Subsequently, n=16
497 ligations were performed using 300 ng of digested and dephosphorylated Trono-BR backbone and 3 ng of
498 digested insert with high concentration T4 DNA Ligase (NEB #M0202M). The ligation reactions were precipitated
499 using QuantaBio 5PRIME Phase Lock Gel tubes before being resuspended in 3 µL of EB Buffer per 4 precipitated
500 reactions. These precipitated ligation reactions were electroporated into Lucigen Endura ElectroCompetent Cells
501 (#60242-2) before being plated on LB-Carbenicillin plates and incubated at 37˚C for 16 hours. Library
502 representation was assessed at this step via serial dilution plating, displaying a representation on the order of
503 400x. We also picked 30 random colonies from these serial dilution plates to assess the fidelity of library cloning
504 and to test a random set of pegRNAs. We scraped the plates and collected the bacteria in 250 mL of LB-Ampicillin
505 per 4 plates, before incubating for 2 hours at 37˚C, spinning the bacteria, and proceeding to perform a Qiagen
506 Maxiprep, following the manufacturer's protocol. Lentivirus was generated via the aforementioned protocol, and
507 viral titer was determined through serial dilutions of virus, transductions in 12-well plates with 1 million A549-
508 PEmax cells, and measurement of the RFP-positive cell fraction at 72-hours post-transduction. For extended
509 protocol information, see **Supplemental Protocol 1.**

510 **Screening protocol:**

511 For each replicate, 110 million A549-PEmax cells were combined with an appropriate amount of p53-sensor
512 virus to achieve an MOI < 1. To this mix, puromycin was added to a final concentration of 10 µg/mL and polybrene
513 transfection reagent (Sigma-Aldrich, catalog no. TR-1003) was added to a final concentration of 8 µg/mL in F-
514 12K (Gibco, catalog no. 21127030**)** media supplemented with 10% FBS and 1X Penicillin-Streptomycin
515 (ThermoFisher). This mix was plated into 9 total 12-well plates per replicate. At 24-hours post-transduction, each

516 12-well plate was expanded to 15-cm plate, with media supplemented with 10 µg/mL puromycin and 10 µg/mL
517 blasticidin S**.** These puromycin and blasticidin S concentrations were maintained throughout the screen. At 72-
518 hours post-transduction, each 15-cm plate was expanded to 2 15-cm plates. At 96-hours post-transduction, each
519 replicate was replated at ≥1000X representation (≥29 million cells) for the untreated arm and the Nutlin-3
520 treatment arm. For the Nutlin-3 treatment arm, Nutlin-3 was added to a final concentration of 10 µM. At this time-
521 point, a cell pellet was taken for gDNA extraction. All cell pellets included ≥29 million cells (1000X representation)
522 and were stored at –80˚C. Subsequently, every 3 days, the cells were split, and replated at 1000X representation.
523 At each time-point, a cell pellet was taken if there were a sufficient number of cells to allow for 1000X
524 representation. This process was repeated until the screen was terminated at Day 34 post-transduction.

525 **Genomic DNA extraction:**

526 Genomic DNA from the Day 4, 16, 25, and 34 time-points was extracted using the Qiagen Genomic Tip/500 G
527 following the manufacturer's protocol. Genomic DNA was resuspended in 200 µL of TE Buffer, pH 8.0.
528 Concentrations were measured using a NanoDrop 2000 (ThermoFisher) and were normalized to 1 ug/uL.

529 **NGS Sample Preparation:**

530 We performed n=30 PCR1 reactions per sample using Q5 High Fidelity 2X Master Mix (NEB #M0429S) with 10
531 ug of genomic DNA to maintain ≥1000X representation. Up to 4 PCR reactions were pooled and PCR purified
532 using the Qiagen PCR purification kit following the manufacturer's protocols. These reactions were then gel
533 purified (Qiagen Gel Extraction Kit), pooled and measured using the NanoDrop 2000 (ThermoFisher). We
534 performed n=4 PCR2 reactions per sample using 10 ng of PCR1 as a template in each reaction. We PCR purified
535 these samples, and then gel purified these samples and eluted in 30 µL of EB Buffer. These samples were then
536 submitted for sequencing. The PCR1 and PCR2 strategies are diagrammed in **Extended Data Fig. 9a.** All
537 primers are deposited in **Supplemental Table 2.**

538 **Next Generation Sequencing (NGS):**

539 We performed Amplicon-EZ sequencing (Azenta) for analysis of the correlation between sensor and endogenous
540 editing **(Fig. 1d).** For the NGS of the p53-sensor library, we used the NovaSeq S1 200 sequencing system

541 (NovaSeq 6000) with a custom sequencing primer set to amplify the protospacer, 3′ extension, sensor sequence,
542 and sample barcode in separate reads. All other NGS data was generated using the Singular G4 Sequencer
543 (2x150 paired-end) with stock primers. All sequencing primers are deposited in **Supplemental Table 2.** The
544 custom sequencing approach for the NovaSeq 6000 is diagrammed in **Extended Data Fig. 9b.**

545 **Golden Gate Assembly of UPEmS pegRNAs for follow-up validation:**

546 For follow-up validation of pegRNAs, individual pegRNAs were cloned via Golden Gate Assembly into the Lenti-
547 UPEmS-tevo backbone (generated by the present study). Golden Gate Assembly was performed with annealed
548 spacer oligonucleotides, annealed and phosphorylated scaffold oligonucleotides, and annealed 3′ extension
549 oligonucleotides using NEB BsmBI Golden Gate Enzyme Mix, before being transformed, mini prepped (Qiagen),
550 and validated via whole-plasmid sequencing (Primordium). For full protocol details, see **Supplemental Protocol**
551 **2**.

552 **Competition assays:**

553 To generate variant p53 lines, we seeded 100K A549-PEmax cells in 6-well plates and added UPEmS lentivirus
554 corresponding to each variant. To achieve saturation editing, we waited 7–10 days, expanding the cells to a 10-
555 cm plate when they reached confluence. At this point, we mixed 250K variant (RFP+) cells with 750K un-
556 transduced A549-PEmax cells, and plated 50K cells in triplicate in 6-well plates. For drug treated conditions
557 (Nutlin-3, COTI-2, PK7088), the compound was added to the appropriate concentration. Remaining cells were
558 used for flow analysis and to generate a t=0 cell pellet. At day 7 and day 14, we assessed the RFP positive
559 fraction of the cells via flow cytometry, and at the final time-point took a cell pellet for gDNA extraction.

560 **<u>Analytic/Computational Methods:</u>**

561 **Selection of *TP53* Variants and prime editing sensor library generation with PEGG:**

562 To select a cohort of *TP53* variants for generating a prime editing sensor library, we used the MSK-IMPACT
563 database[20]. We chose all SNVs observed in patients, as well as a collection of observed and random indels to

564 increase the diversity of edits **(Extended Data Fig. 1b)**. In addition, PEGG automatically generated 95
565 neutral/silent variants that tiled the *TP53* locus to act as internal controls in the screen.

566 PEGG generated a maximum of 30 ranked pegRNA designs per variant with RTT lengths of 10, 15, 20, 25, and
567 30 nt, and PBS lengths of 10, 13, and 15 nt coupled to "NGG" protospacers. A "G" was appended to the start of
568 each 20 nt protospacer to improve U6 promoter-mediated transcription. After PEGG generated these pegRNA
569 designs, we further filtered the library to exclude pegRNAs containing polyT termination sequences (≥ 4
570 consecutive Ts), EcoRI and Esp3I sites, and protospacers with an MIT specificity score less than 50. In addition,
571 each pegRNA oligo included a matched, 60 nt sensor locus that was automatically generated by PEGG and
572 used to link each pegRNA to its editing outcome.

573 For full details of generating a prime editing sensor library using PEGG, visit pegg.readthedocs.io.

574 **Analysis of the p53-sensor screen:**

575 The p53-sensor sequencing results were demultiplexed into separate fastq files based on the sample barcode.
576 Next, using a custom analysis script, we filtered reads with an average Phred quality score below 30, and
577 identified pegRNAs based on the protospacer and 3′ extension sequences. Sequences with no matching
578 protospacer or 3′ extension were discarded, and sequences with mismatched protospacer and 3′ extension
579 sequences were discarded and classified as recombination events. Sequences with matching protospacer and
580 3′ extension sequences were used to generate pegRNA counts tables that were subsequently used for MAGeCK
581 analysis of pegRNA enrichment/depletion.

582 To classify editing outcomes at the sensor locus, we first determined whether recombination had occurred to
583 decouple the pegRNA from its matched target sequence. To do so, we used the first and last 5-nt of the sensor
584 sequence as a barcode to detect recombination. Sensor reads with the first and last 5-nt of the read matching
585 the appropriate pegRNA were classified as correct sensor reads, while those with the first and last 5-nt matching
586 other pegRNAs were classified as recombination events and discarded. We noted that recombination between
587 the pegRNA and sensor was observed at a significantly higher rate when the protospacer was in the same
588 orientation as the sensor, prompting us to update PEGG to automatically place the sensor sequence in the

589 reverse orientation to reduce recombination in future PE sensor libraries. **(Extended Data Fig. 2e, 2f).** Reads
590 with the first and last 5-nt with no match were classified as potential indels and retained. For each sample, the
591 sensor reads that were not recombined were demultiplexed into separate fastq files for each pegRNA. We then
592 used Crispresso2[69] to classify editing outcomes, excluding the first and last 5-nt of the sensor read from the
593 quantification window. To determine the background subtracted correct editing %, we subtracted the correct
594 editing % observed in the plasmid library from the correct editing % observed at a given time-point, although we
595 note that for plasmids with at least 10 sensor reads, the median correct editing % was 0%, the average correct
596 editing % was < 0.1%, and the max observed correct editing % was 8.7%.

597 For analysis of enrichment/depletion of pegRNAs, we used the MAGeCK algorithm[47], with the Day 4 sample
598 designated as the control time-point. We then filtered to exclude pegRNAs with a control count mean <10 reads
599 to reduce spuriously enriching pegRNA hits. For direct comparison with the cDNA libraries, the LFC values
600 produced by MAGeCK were transformed into Z-Scores using the standard Z-score formula including all
601 pegRNAs under consideration.

602 **Processing and Analysis of *TP53* NGS Sequencing:**

603 The sequencing files were automatically demultiplexed into separate fastq files based on the sample barcode
604 (12 total samples). Next, we trimmed the sequences from 150 nucleotides to 100 nucleotides, to allow the
605 sequences to be joined. The sequences were joined using the fastq-join algorithm with the default parameters
606 enabled[70]. We then used custom analysis scripts to generate counts tables for all of the unique sequences,
607 merge matching samples from different flow cells, and determine the HGVSp and HGVSc of each sequence.

608 To determine the LFC of each variant at these endogenous loci, we first filtered to exclude undesired variants
609 (i.e. those not targeted by pegRNAs in the library) and created counts tables for Day 4, Day 34 (untreated) and
610 Day 34 (Nutlin-treated) for each of the three amplicons. For each amplicon, we used MAGeCK to normalize read
611 counts between samples and determine the LFC of each variant. We then filtered endogenous variants with a
612 control count <10 reads to reduce spuriously enriching variants. These MAGeCK tables from the different
613 amplicons were concatenated to perform downstream analysis, comparing the endogenous variants with the

614 pegRNA–sensor sequencing results. In addition, we performed sequencing of the WT A549 PEmax cell line,
615 which confirmed the WT status of the regions amplified.

616 **Data Availability:**

617 Raw sequencing data from the screen is deposited in the SRA under accession PRJNA1014453. All processed
618 datasets, analysis scripts, as well as Jupyter notebooks and source data for generating each figure that appears
619 in the paper, are available at the following GitHub repository: https://github.com/samgould2/p53-prime-editing-
620 sensor**.** Further documentation and installation instructions for PEGG are available at pegg.readthedocs.io**.**

621 **Data Tables:**

622 - **Supplemental Table 1:** pegRNAs & variant information
623 - **Supplemental Table 2:** Primers
624 - **Supplemental Protocol 1:** Cloning of p53 PE sensor libraries
625 - **Supplemental Protocol 2:** Golden Gate Assembly of pegRNAs in Lenti-UPEmS-tevo backbone
626 - Other information and source data are provided in the Github Repository**.**

627 **Acknowledgements:**

628 We dedicate this work in memory of Jingzhi Zhu, a research computing specialist at the Koch Institute Integrated
629 Genomics and Bioinformatics Core who worked tirelessly to ensure that our community had a robust computing
630 infrastructure. We thank Nicolas Mathey-Andrews, Carol L. Prives, Michael T. Hemann, Jonathan S. Weissman,
631 Luke W. Koblan, and Lukas Dow for excellent scientific discussions and overall support. S.I.G. was supported
632 by T32GM136540 and the MIT School of Science Fellowship in Cancer Research. F.J.S.R. is an HHMI Hanna
633 Gray Fellow and was supported by the V Foundation for Cancer Research (V2022-028), NCI Cancer Center
634 Support Grant P30-CA1405, the Ludwig Center at MIT (2036636), Koch Institute Frontier Awards (2036648 and
635 2036642) and the MIT Research Support Committee (3189800). This work was also supported in part by the
636 Koch Institute Support (core) Grant P30-CA14051 from the National Cancer Institute. We also thank the Koch

637 Institute Swanson Biotechnology Center for technical support, especially the Flow Cytometry Core, the Barbara
638 K. Ostrom (1978) Bioinformatics Facility, and the Genomics Facility. A.H. is a National Science Foundation (NSF)
639 Graduate Research Fellow. A.H. and D.R.L. were supported by NIH U01AI142756, R35GM118062,
640 RM1HG009490, and HHMI. This article is subject to HHMI's Open Access to Publications policy. HHMI lab heads
641 have previously granted a nonexclusive CC BY 4.0 license to the public and a sublicensable license to HHMI in
642 their research articles. Pursuant to those licenses, the author-accepted manuscript of this article can be made
643 freely available under a CC BY 4.0 license immediately upon publication.

644 **Author Contributions:**

645 S.I.G. and F.J.S.R. conceived the project and wrote the manuscript. S.I.G. performed all computational analyses
646 and analyzed experimental data. S.I.G., A.N.W., K.D., and G.A.J. performed experiments. G.A.J. generated
647 Lenti-PEAR-mCherry. V.K.N. generated Lenti-EFS-PEmax-P2A-Puro. S.S.L. assisted in designing sequencing
648 strategy and performing next-generation sequencing. A.H. and D.R.L. provided conceptual and technical advice
649 and comments on the manuscript. F.J.S.R. supervised the work and secured funding.

650 **Competing Interests:**

651 The authors declare competing financial interests: D.R.L. is a consultant and/or equity owner for Prime Medicine,
652 Beam Therapeutics, Pairwise Plants, Chroma Medicine, and Nvelop Therapeutics, companies that use or deliver
653 genome editing or epigenome engineering agents.

654 **References:**

655 1. Winters, I. P. *et al.* Multiplexed in vivo homology-directed repair and tumor barcoding enables parallel
656 quantification of Kras variant oncogenicity. *Nat. Commun.* **8**, 2053 (2017).
657 2. Boettcher, S. *et al.* A dominant-negative effect drives selection of TP53 missense mutations in myeloid
658 malignancies. *Science* **365**, 599–604 (2019).
659 3. Sharon, E. *et al.* Functional Genetic Variants Revealed by Massively Parallel Precise Genome Editing. *Cell*
660 **175**, 544-557.e16 (2018).
661 4. Findlay, G. M., Boyle, E. A., Hause, R. J., Klein, J. C. & Shendure, J. Saturation editing of genomic regions

662 by multiplex homology-directed repair. *Nature* **513**, 120–123 (2014).

663 5. Findlay, G. M. *et al.* Accurate classification of BRCA1 variants with saturation genome editing. *Nature* **562**,
664 217–222 (2018).

665 6. Giacomelli, A. O. *et al.* Mutational processes shape the landscape of TP53 mutations in human cancer. *Nat.*
666 *Genet.* **50**, 1381–1387 (2018).

667 7. Kotler, E. *et al.* A Systematic p53 Mutation Library Links Differential Functional Impact to Cancer Mutation
668 Pattern and Evolutionary Conservation. *Mol. Cell* **71**, 178-190.e8 (2018).

669 8. Komor, A. C., Kim, Y. B., Packer, M. S., Zuris, J. A. & Liu, D. R. Programmable editing of a target base in
670 genomic DNA without double-stranded DNA cleavage. *Nature* **533**, 420–424 (2016).

671 9. Gaudelli, N. M. *et al.* Programmable base editing of A•T to G•C in genomic DNA without DNA cleavage.
672 *Nature* **551**, 464–471 (2017).

673 10. Anzalone, A. V. *et al.* Search-and-replace genome editing without double-strand breaks or donor DNA.
674 *Nature* **576**, 149–157 (2019).

675 11. Erwood, S. *et al.* Saturation variant interpretation using CRISPR prime editing. *Nat. Biotechnol.* **40**, 885–
676 895 (2022).

677 12. Ren, X. *et al.* High throughput PRIME editing screens identify functional DNA variants in the human genome.
678 *bioRxiv* 2023.07.12.548736 (2023) doi:10.1101/2023.07.12.548736.

679 13. Chardon, F. M. *et al.* A multiplex, prime editing framework for identifying drug resistance variants at scale.
680 *bioRxiv* 2023.07.27.550902 (2023) doi:10.1101/2023.07.27.550902.

681 14. Sánchez-Rivera, F. J. *et al.* Base editing sensor libraries for high-throughput engineering and functional
682 analysis of cancer-associated single nucleotide variants. *Nat. Biotechnol.* **40**, 862–873 (2022).

683 15. Kato, S. *et al.* Understanding the function-structure and function-mutation relationships of p53 tumor
684 suppressor protein by high-resolution missense mutation analysis. *Proc. Natl. Acad. Sci. U. S. A.* **100**, 8424–
685 8429 (2003).

686 16. Ursu, O. *et al.* Massively parallel phenotyping of coding variants in cancer with Perturb-seq. *Nat. Biotechnol.*
687 **40**, 896–905 (2022).

688 17. Kastenhuber, E. R. & Lowe, S. W. Putting p53 in Context. *Cell* **170**, 1062–1078 (2017).

689 18. Gencel-Augusto, J. & Lozano, G. p53 tetramerization: at the center of the dominant-negative effect of mutant
690 p53. *Genes Dev.* **34**, 1128–1146 (2020).
691 19. Baugh, E. H., Ke, H., Levine, A. J., Bonneau, R. A. & Chan, C. S. Why are there hotspot mutations in the
692 TP53 gene in human cancers? *Cell Death Differ.* **25**, 154–160 (2018).
693 20. Zehir, A. *et al.* Mutational landscape of metastatic cancer revealed from prospective clinical sequencing of
694 10,000 patients. *Nat. Med.* **23**, 703–713 (2017).
695 21. Chen, P. J. *et al.* Enhanced prime editing systems by manipulating cellular determinants of editing
696 outcomes. *Cell* **184**, 5635-5652.e29 (2021).
697 22. Nelson, J. W. *et al.* Engineered pegRNAs improve prime editing efficiency. *Nat. Biotechnol.* **40**, 402–410
698 (2022).
699 23. Doman, J. L. *et al.* Phage-assisted evolution and protein engineering yield compact, efficient prime editors.
700 *Cell* **186**, 3983-4002.e26 (2023).
701 24. Morris, J. A., Rahman, J. A., Guo, X. & Sanjana, N. E. Automated design of CRISPR prime editors for 56,000
702 human pathogenic variants. *iScience* **24**, 103380 (2021).
703 25. Li, Y., Chen, J., Tsai, S. Q. & Cheng, Y. Easy-Prime: a machine learning-based prime editor design tool.
704 *Genome Biol.* **22**, 235 (2021).
705 26. Chow, R. D., Chen, J. S., Shen, J. & Chen, S. A web tool for the design of prime-editing guide RNAs. *Nat*
706 *Biomed Eng* **5**, 190–194 (2021).
707 27. Hsu, J. Y. *et al.* PrimeDesign software for rapid and simplified design of prime editing guide RNAs. *Nat.*
708 *Commun.* **12**, 1034 (2021).
709 28. Anderson, M. V., Haldrup, J., Thomsen, E. A., Wolff, J. H. & Mikkelsen, J. G. pegIT - a web-based design
710 tool for prime editing. *Nucleic Acids Res.* **49**, W505–W509 (2021).
711 29. Hwang, G.-H. *et al.* PE-Designer and PE-Analyzer: web-based design and analysis tools for CRISPR prime
712 editing. *Nucleic Acids Res.* **49**, W499–W504 (2021).
713 30. Standage-Beier, K., Tekel, S. J., Brafman, D. A. & Wang, X. Prime Editing Guide RNA Design Automation
714 Using PINE-CONE. *ACS Synth. Biol.* **10**, 422–427 (2021).
715 31. Bhagwat, A. M. *et al.* multicrispr: gRNA design for prime editing and parallel targeting of thousands of

716 targets. *Life Sci Alliance* **3**, (2020).

717 32. Mathis, N. *et al.* Predicting prime editing efficiency and product purity by deep learning. *Nat. Biotechnol.*
718 (2023) doi:10.1038/s41587-022-01613-7.

719 33. Yu, G. *et al.* Prediction of efficiencies for diverse prime editing systems in multiple cell types. *Cell* **186**, 2256-
720 2272.e23 (2023).

721 34. Kim, Y. *et al.* High-throughput functional evaluation of human cancer-associated mutations using base
722 editors. *Nat. Biotechnol.* **40**, 874–884 (2022).

723 35. Marquart, K. F. *et al.* Predicting base editing outcomes with an attention-based deep learning algorithm
724 trained on high-throughput target library screens. *Nat. Commun.* **12**, 5114 (2021).

725 36. Arbab, M. *et al.* Determinants of Base Editing Outcomes from Target Library Analysis and Machine Learning.
726 *Cell* **182**, 463-480.e30 (2020).

727 37. Kim, H. K. *et al.* Predicting the efficiency of prime editing guide RNAs in human cells. *Nat. Biotechnol.* **39**,
728 198–206 (2021).

729 38. Gould, S. I. & Sánchez-Rivera, F. J. PEGG: A computational pipeline for rapid design of prime editing guide
730 RNAs and sensor libraries. *bioRxiv* 2022.10.26.513842 (2022) doi:10.1101/2022.10.26.513842.

731 39. Cerami, E. *et al.* The cBio cancer genomics portal: an open platform for exploring multidimensional cancer
732 genomics data. *Cancer Discov.* **2**, 401–404 (2012).

733 40. Landrum, M. J. *et al.* ClinVar: improving access to variant interpretations and supporting evidence. *Nucleic*
734 *Acids Res.* **46**, D1062–D1067 (2018).

735 41. Hsu, P. D. *et al.* DNA targeting specificity of RNA-guided Cas9 nucleases. *Nat. Biotechnol.* **31**, 827–832
736 (2013).

737 42. Li, X. *et al.* Chromatin context-dependent regulation and epigenetic manipulation of prime editing. *bioRxiv*
738 2023.04.12.536587 (2023) doi:10.1101/2023.04.12.536587.

739 43. Simon, D. A. *et al.* PEAR, a flexible fluorescent reporter for the identification and enrichment of successfully
740 prime edited cells. *Elife* **11**, (2022).

741 44. Vassilev, L. T. *et al.* In vivo activation of the p53 pathway by small-molecule antagonists of MDM2. *Science*
742 **303**, 844–848 (2004).

743 45. Koeppel, J. *et al.* Prediction of prime editing insertion efficiencies using sequence features and DNA repair
744 determinants. *Nat. Biotechnol.* (2023) doi:10.1038/s41587-023-01678-y.
745 46. Doench, J. G. *et al.* Optimized sgRNA design to maximize activity and minimize off-target effects of CRISPR-
746 Cas9. *Nat. Biotechnol.* **34**, 184–191 (2016).
747 47. Li, W. *et al.* MAGeCK enables robust identification of essential genes from genome-scale CRISPR/Cas9
748 knockout screens. *Genome Biol.* **15**, 554 (2014).
749 48. de Andrade, K. C. *et al.* The TP53 Database: transition from the International Agency for Research on
750 Cancer to the US National Cancer Institute. *Cell Death Differ.* **29**, 1071–1073 (2022).
751 49. Kircher, M. *et al.* A general framework for estimating the relative pathogenicity of human genetic variants.
752 *Nat. Genet.* **46**, 310–315 (2014).
753 50. Hong, D. S. *et al.* KRASG12C Inhibition with Sotorasib in Advanced Solid Tumors. *N. Engl. J. Med.* **383**,
754 1207–1217 (2020).
755 51. Salim, K. Y., Maleki Vareki, S., Danter, W. R. & Koropatnick, J. COTI-2, a novel small molecule that is active
756 against multiple human cancer cell lines in vitro and in vivo. *Oncotarget* **7**, 41363–41379 (2016).
757 52. Lindemann, A. *et al.* COTI-2, A Novel Thiosemicarbazone Derivative, Exhibits Antitumor Activity in HNSCC
758 through p53-dependent and -independent Mechanisms. *Clin. Cancer Res.* **25**, 5650–5662 (2019).
759 53. Liu, X. *et al.* Small molecule induced reactivation of mutant p53 in cancer cells. *Nucleic Acids Res.* **41**, 6034–
760 6044 (2013).
761 54. Song, H. *et al.* Diverse rescue potencies of p53 mutations to ATO are predetermined by intrinsic mutational
762 properties. *Sci. Transl. Med.* **15**, eabn9155 (2023).
763 55. Muller, P. A. J. & Vousden, K. H. Mutant p53 in cancer: new functions and therapeutic opportunities. *Cancer*
764 *Cell* **25**, 304–317 (2014).
765 56. Loizou, E. *et al.* A Gain-of-Function p53-Mutant Oncogene Promotes Cell Fate Plasticity and Myeloid
766 Leukemia through the Pluripotency Factor FOXH1. *Cancer Discov.* **9**, 962–979 (2019).
767 57. Alexandrova, E. M. *et al.* Improving survival by exploiting tumour dependence on stabilized mutant p53 for
768 treatment. *Nature* **523**, 352–356 (2015).
769 58. Schulz-Heddergott, R. *et al.* Therapeutic Ablation of Gain-of-Function Mutant p53 in Colorectal Cancer

770 Inhibits Stat3-Mediated Tumor Growth and Invasion. *Cancer Cell* **34**, 298-314.e7 (2018).

771 59. Olive, K. P. *et al.* Mutant p53 gain of function in two mouse models of Li-Fraumeni syndrome. *Cell* **119**, 847–
772 860 (2004).

773 60. Lang, G. A. *et al.* Gain of function of a p53 hot spot mutation in a mouse model of Li-Fraumeni syndrome.
774 *Cell* **119**, 861–872 (2004).

775 61. Freed-Pastor, W. A. *et al.* Mutant p53 disrupts mammary tissue architecture via the mevalonate pathway.
776 *Cell* **148**, 244–258 (2012).

777 62. Weissmueller, S. *et al.* Mutant p53 drives pancreatic cancer metastasis through cell-autonomous PDGF
778 receptor β signaling. *Cell* **157**, 382–394 (2014).

779 63. Choe, J. H. *et al.* Li-Fraumeni Syndrome-Associated Dimer-Forming Mutant p53 Promotes Transactivation-
780 Independent Mitochondrial Cell Death. *Cancer discovery* vol. 13 1250–1273 (2023).

781 64. Gencel-Augusto, J. *et al.* Dimeric p53 Mutant Elicits Unique Tumor-Suppressive Activities through an Altered
782 Metabolic Program. *Cancer discovery* vol. 13 1230–1249 (2023).

783 65. Clore, G. M. *et al.* High-resolution structure of the oligomerization domain of p53 by multidimensional NMR.
784 *Science* **265**, 386–391 (1994).

785 66. Ely, Z. A. *et al.* A prime editor mouse to model a broad spectrum of somatic mutations in vivo. *Nat.*
786 *Biotechnol.* (2023) doi:10.1038/s41587-023-01783-y.

787 67. Akama-Garren, E. H. *et al.* A Modular Assembly Platform for Rapid Generation of DNA Constructs. *Sci.*
788 *Rep.* **6**, 16836 (2016).

789 68. Wiznerowicz, M. & Trono, D. Conditional suppression of cellular genes: lentivirus vector-mediated drug-
790 inducible RNA interference. *J. Virol.* **77**, 8957–8961 (2003).

791 69. Clement, K. *et al.* CRISPResso2 provides accurate and rapid genome editing sequence analysis. *Nat.*
792 *Biotechnol.* **37**, 224–226 (2019).

793 70. Aronesty, E. Comparison of sequencing utility programs. *Open Bioinforma. J.* **7**, 1–8 (2013).

794

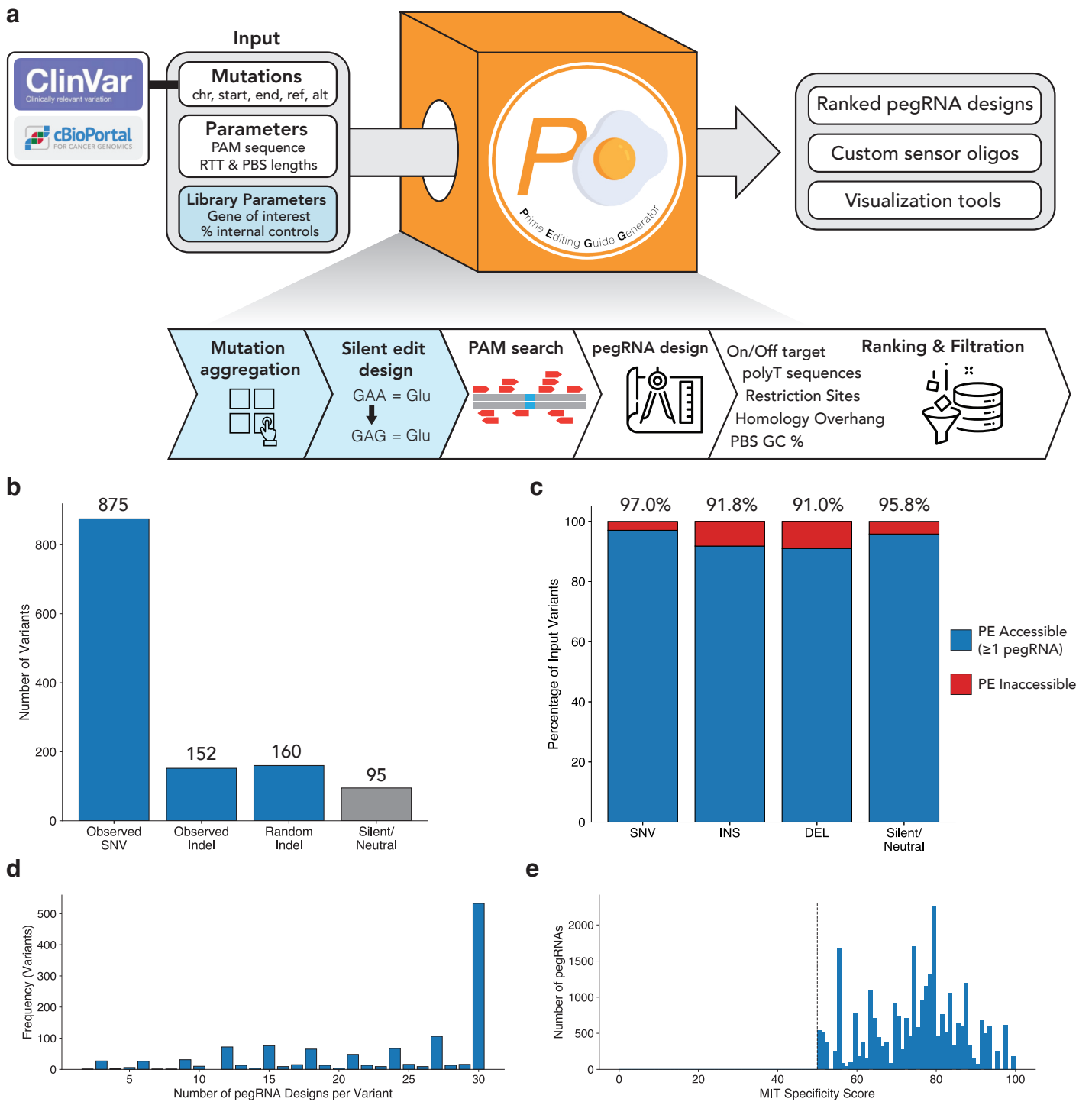

Extended Data Fig. 1 | Generation of a TP53 prime editing sensor library with PEGG. a, Schematic of the PEGG pipeline. PEGG takes as input a list of mutations from the cBioPortal, ClinVar identifiers, or custom mutations sets, and produces user-defined pegRNA designs ranked by PEGG score, custom sensor oligos, and visualization tools. PEGG filters pegRNAs with polyT sequences as well as designs containing restriction sites used for cloning. With the library design feature, PEGG can also automate the aggregation of variants located in genes of interest, and automatically design a defined fraction of silent variant-generating pegRNAs. **b,** Breakdown of the TP53 variants input to PEGG for sensory library design. **c,** The fraction of input variants amenable to prime editing (i.e., able to generate ≥ 1 pegRNA), separated by variant type. **d,** Histogram of the number of pegRNA designs per variant. **e,** Histogram of the MIT specificity score of the protospacers for the pegRNAs included in the library. The library was filtered to exclude pegRNAs containing a protospacer with an MIT specificity score less than 50.

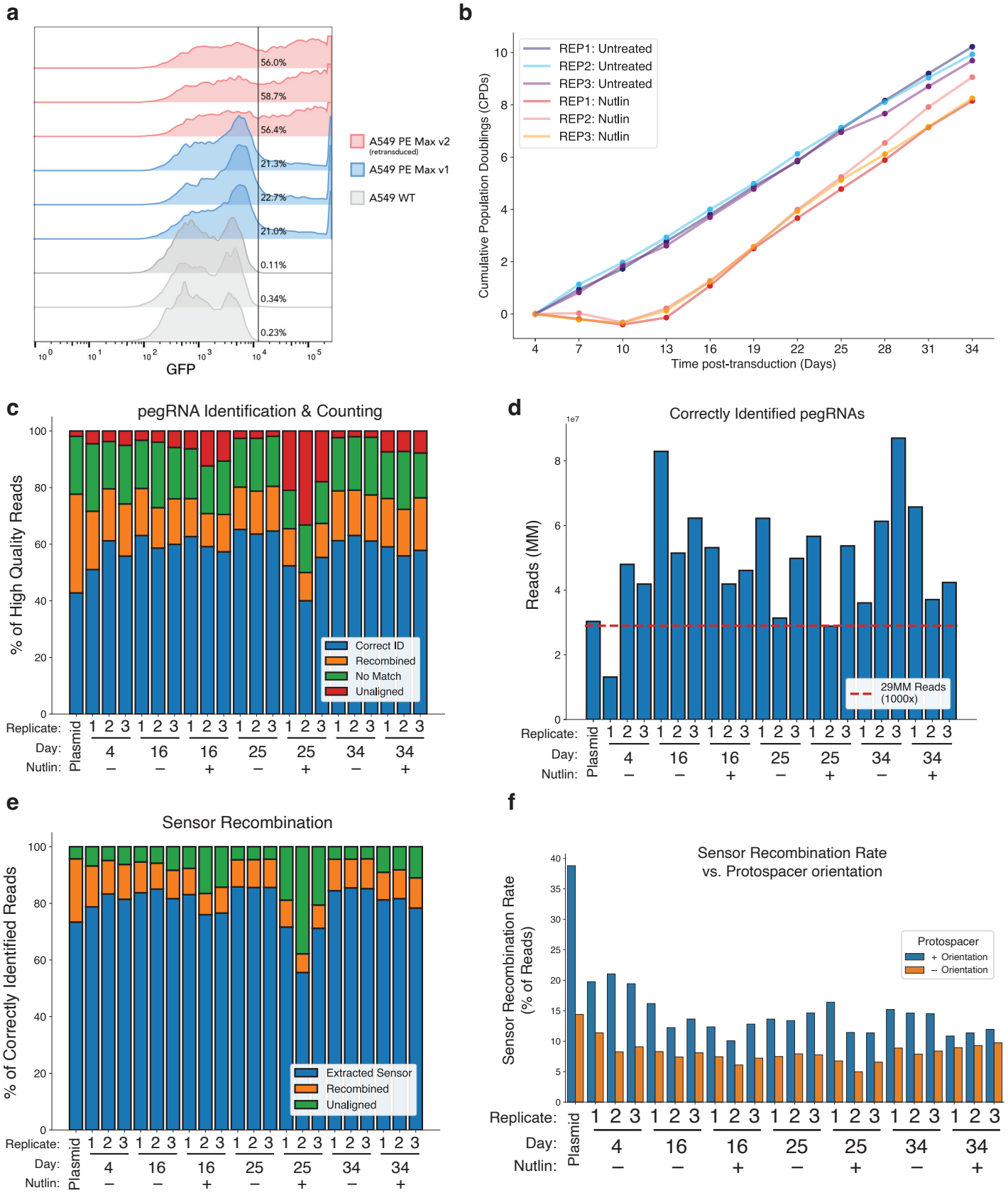
a
56.0%
58.7%
56.4%
21.3%
22.7%
21.0%
0.11%
0.34%
0.23%
A549 PE Max v2 (retransduced)
A549 PE Max v1
A549 WT
GFP
b
REP1: Untreated
REP2: Untreated
REP3: Untreated
REP1: Nutlin
REP2: Nutlin
REP3: Nutlin
Cumulative Population Doublings (CPDs)
Time post-transduction (Days)
c
pegRNA Identification & Counting
% of High Quality Reads
Correct ID
Recombined
No Match
Unaligned
Replicate:
Day:
Nutlin:
Plasmid
d
Correctly Identified pegRNAs
Reads (MM)
29MM Reads (1000x)
e
Sensor Recombination
% of Correctly Identified Reads
Extracted Sensor
Recombined
Unaligned
f
Sensor Recombination Rate vs. Protospacer orientation
Sensor Recombination Rate (% of Reads)
Protospacer
+ Orientation
– Orientation

Extended Data Fig. 2 | Optimization, screening, and deconvolution of the *TP53* prime editing sensor library. a, Assessment of the prime editing activity of A549-PEmax cell lines using a modified all-in-one PEAR reporter, where GFP is turned on in the event of successful prime editing. Three replicates each of A549 WT (gray), A549-PEmax v1 (blue), which underwent a single transduction with EFS-PEmax-P2A-Puro, and A549-PEmax v2 (pink), which underwent multiple rounds of transduction with EFS-PEmax-P2A-Puro, are shown, along with the quantification of GFP-positive cells. **b,** Cumulative population doublings during the course of the screen of each of the replicates in the untreated and Nutlin-treated conditions. **c,** Identification and counting of pegRNAs in each replicate and time-point from high quality reads (Q > 30). Correct ID = reads with matching protospacer and 3' extension. Recombined = reads with mismatched protospacer and 3' extension. No match = reads with no matching sequence for protospacer or 3' extension. Unaligned = reads with no identifiable tevopreQ1 sequence. Plasmid = Plasmid Library. **d,** Count of correctly identified pegRNAs in each replicate and time-point. **e,** Extraction of the sensor locus from reads with correctly identified pegRNAs. Extracted sensor = sensor read matches pegRNA identification and is thus extracted and saved. Recombined = sensor read does not match pegRNA (discarded). Unaligned = no polyT-tevopreQ1 sequence found. **f,** Sensor recombination rate as a function of protospacer orientation. When the protospacer is on the positive strand (+) of the sensor (blue), the recombination rate increases compared to when the protospacer is on the negative strand (-) of the sensor.

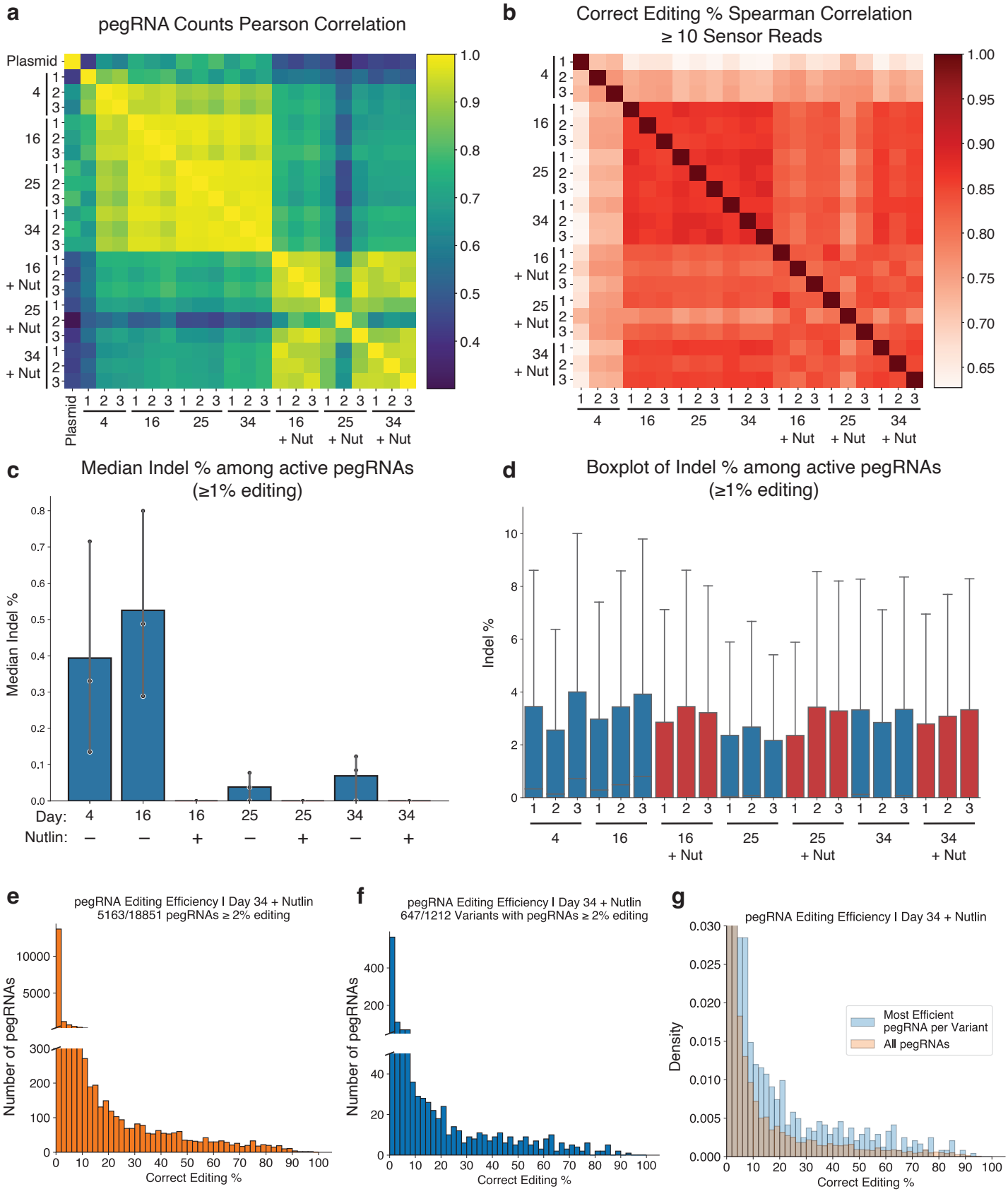
a
pegRNA Counts Pearson Correlation
Plasmid
4
16
25
34
16 + Nut
25 + Nut
34 + Nut
1.0
0.9
0.8
0.7
0.6
0.5
0.4
b
Correct Editing % Spearman Correlation
≥ 10 Sensor Reads
1.00
0.95
0.90
0.85
0.80
0.75
0.70
0.65
c
Median Indel % among active pegRNAs
(≥1% editing)
Median Indel %
Day: 4 16 16 25 25 34 34
Nutlin: – – + – + – +
d
Boxplot of Indel % among active pegRNAs
(≥1% editing)
Indel %
e
pegRNA Editing Efficiency I Day 34 + Nutlin
5163/18851 pegRNAs ≥ 2% editing
Number of pegRNAs
Correct Editing %
f
pegRNA Editing Efficiency I Day 34 + Nutlin
647/1212 Variants with pegRNAs ≥ 2% editing
Number of pegRNAs
Correct Editing %
g
pegRNA Editing Efficiency I Day 34 + Nutlin
Density
Most Efficient pegRNA per Variant
All pegRNAs
Correct Editing %

Extended Data Fig. 3 | The *TP53* prime editing sensor screen is highly reproducible with low indel rates. a, Pearson correlation in raw pegRNA counts among each replicate and time-point. Plasmid = plasmid library. **b,** Spearman correlation in sensor correct editing percentage among each replicate and time-point for pegRNAs with at least 10 sensor reads. **c,** Median indel percentage among active pegRNAs (≥1% editing) for each time-point and condition. **d,** Boxplot of indel frequency among active pegRNAs (≥1% editing) for each replicate and time-point. Lower quartile = 0% for all replicates (not visible). **e,** Histogram of pegRNA editing efficiency in the Nutlin-treated Day 34 samples. **f,** Histogram of pegRNA editing efficiency of the most efficient pegRNA for each variant in the Nutlin-treated Day 34 samples. **g,** Comparative PDF of all pegRNAs and the most efficient pegRNA for each variant.

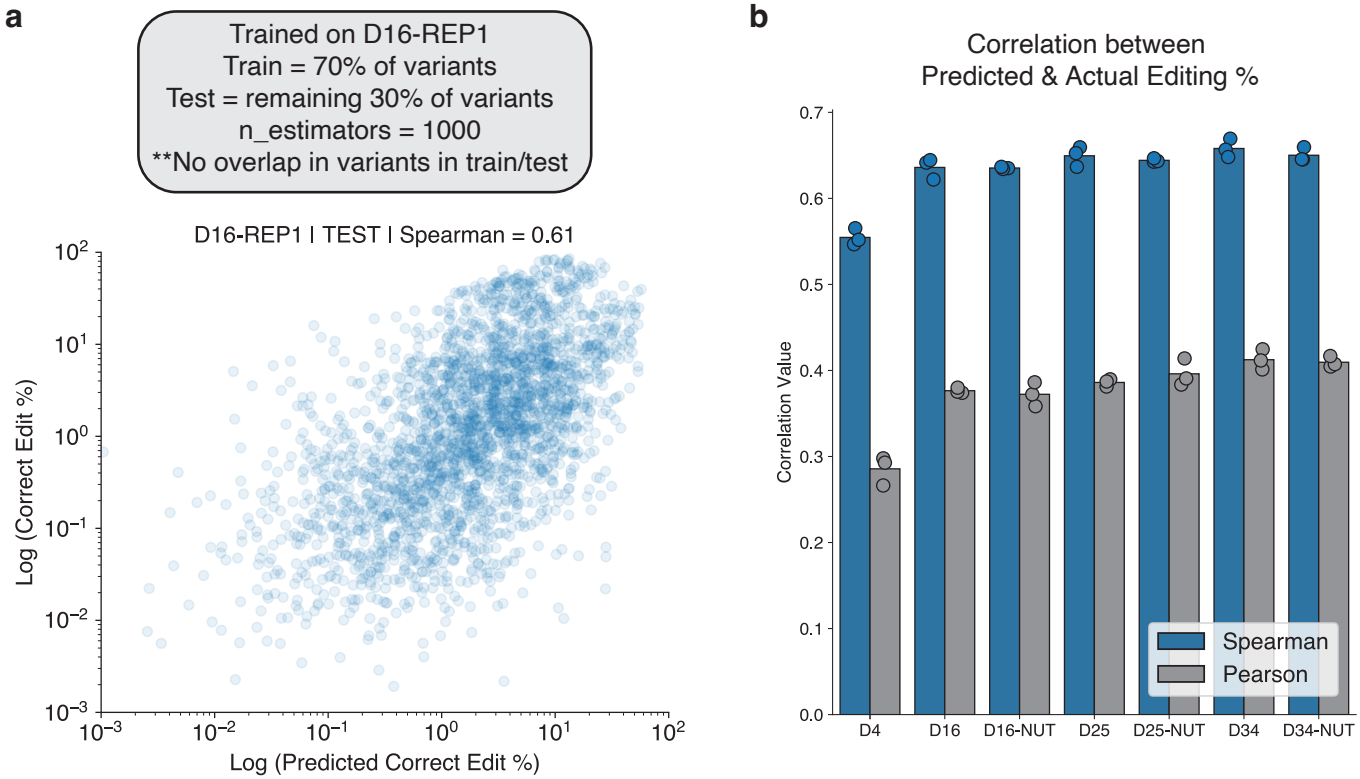

Extended Data Fig. 4 | Training a random forest regressor to predict pegRNA efficiency. a, A random forest regressor was trained on a restricted set of pegRNA features using 70% of the variants in the untreated condition of Day 16 replicate 1. There was no overlap between the variants used for training and testing. The performance on the held-out test set is shown (spearman correlation = 0.61). **b,** Assessment of the performance of the random forest regressor in predicting editing activity at each time-point. Again, only variants in the test set are considered. Each dot represents a separate replicate. Spearman correlation between predicted and actual editing is shown in blue, pearson correlation in gray.

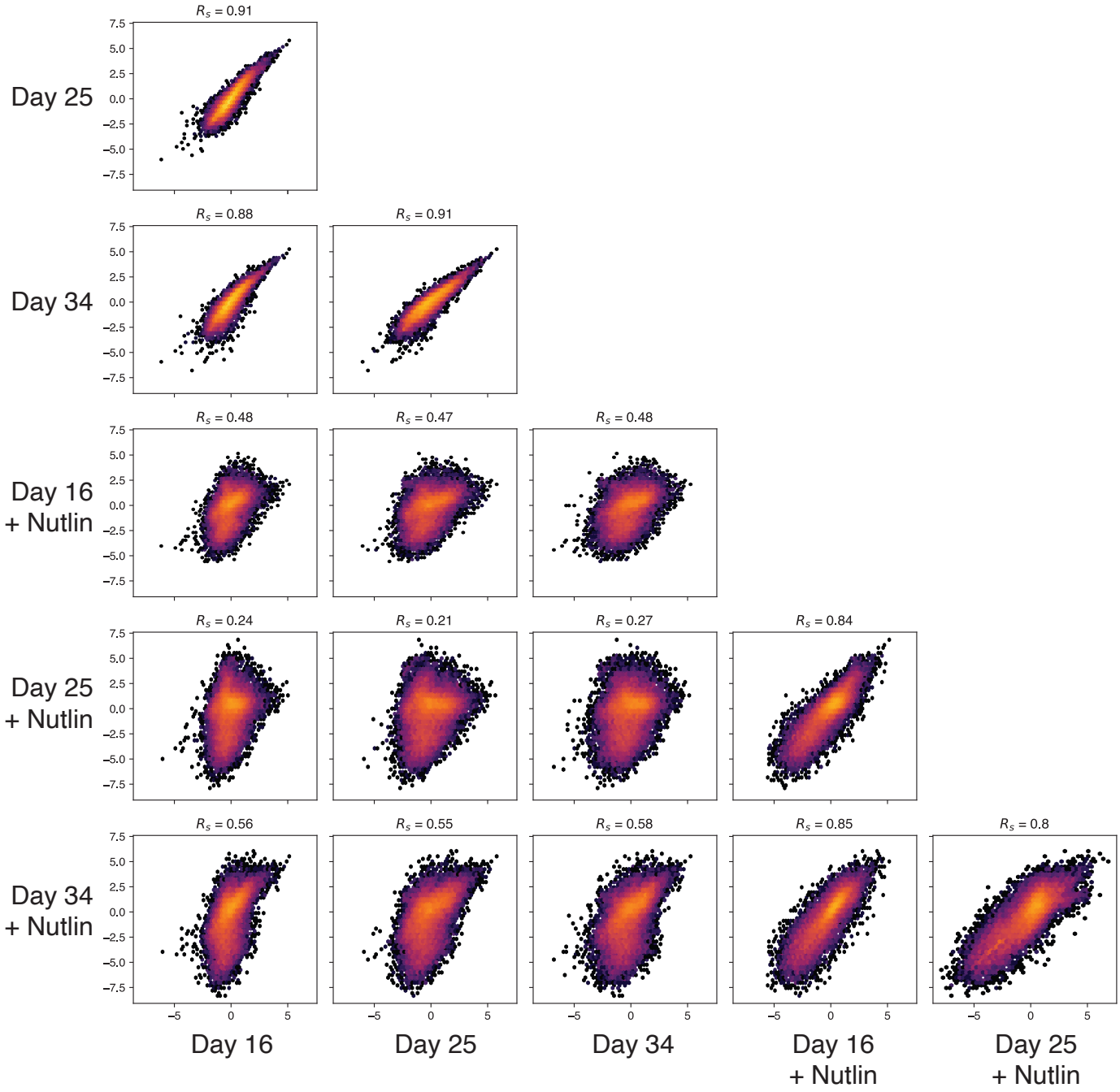

Extended Data Fig. 5 | Correlation in pegRNA LFC among conditions and time-points. Each panel is a density plot of the LFC in pegRNAs at each time-point/condition (i.e. x-axis = LFC of the pegRNAs corresponding with that column's sample, and y-axis = LFC of the pegRNAs corresponding with that row's samples). Replicates were merged using MAGeCK to generate a single (median) LFC for each pegRNA at each time-point. Rs = spearman correlation.

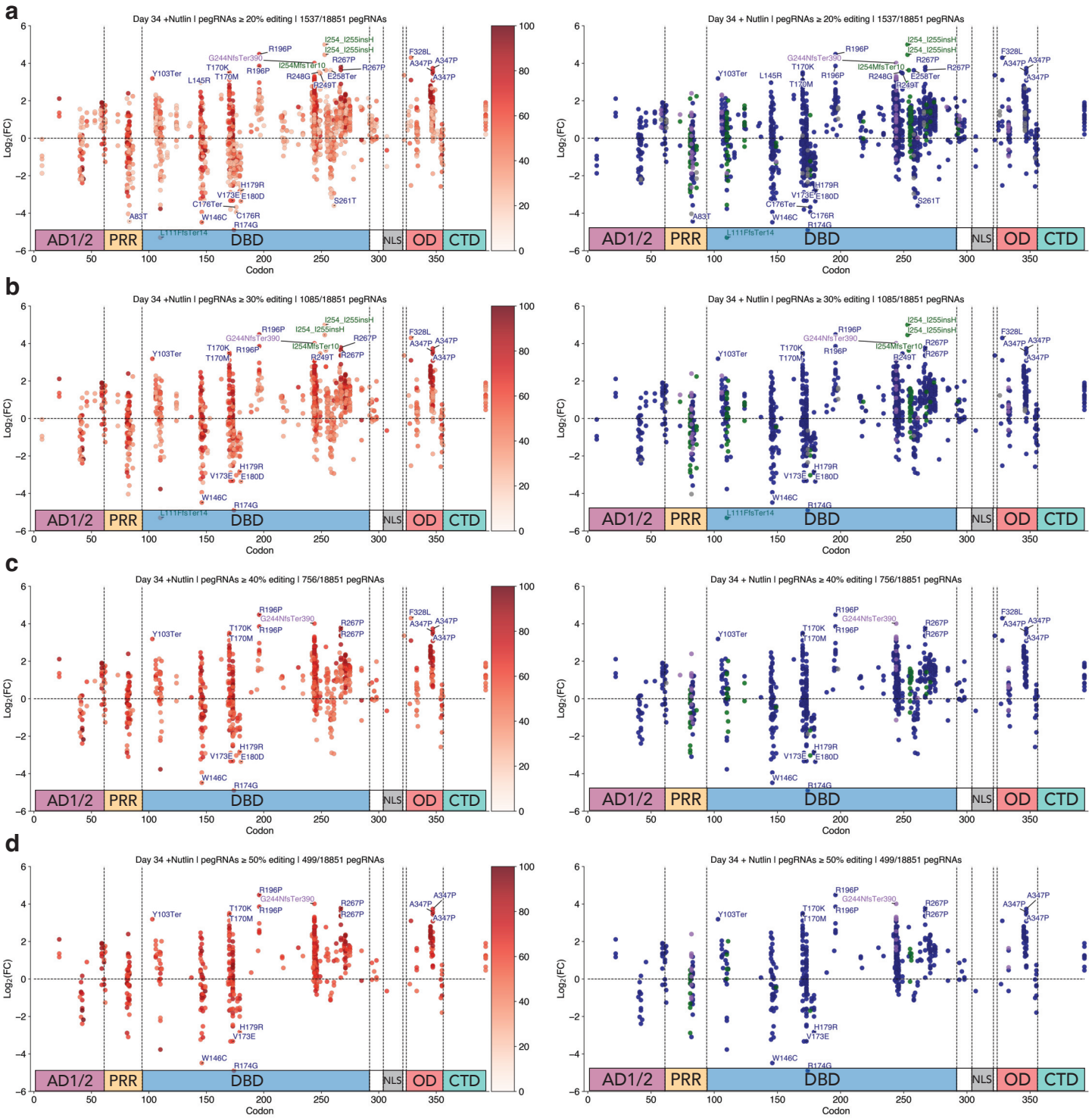

Extended Data Fig. 6 | Filtration of screening data by sensor editing efficiency. The LFC of **a,** pegRNAs ≥ 20% editing **b,** pegRNAs ≥ 30% editing **c,** pegRNAs ≥ 40% editing **d,** pegRNAs ≥ 50% editing, with at least 10 sensor reads at Day 34 relative to Day 4 in the Nutlin-treated condition, with pegRNAs colored by editing efficiency (left) and colored by variant type (right). Selected enriching pegRNAs with FDR < .05 labeled and depleting pegRNAs with FDR < .05 labeled. Blue = SNV, Green = INS, Purple = DEL, Gray = Silent.

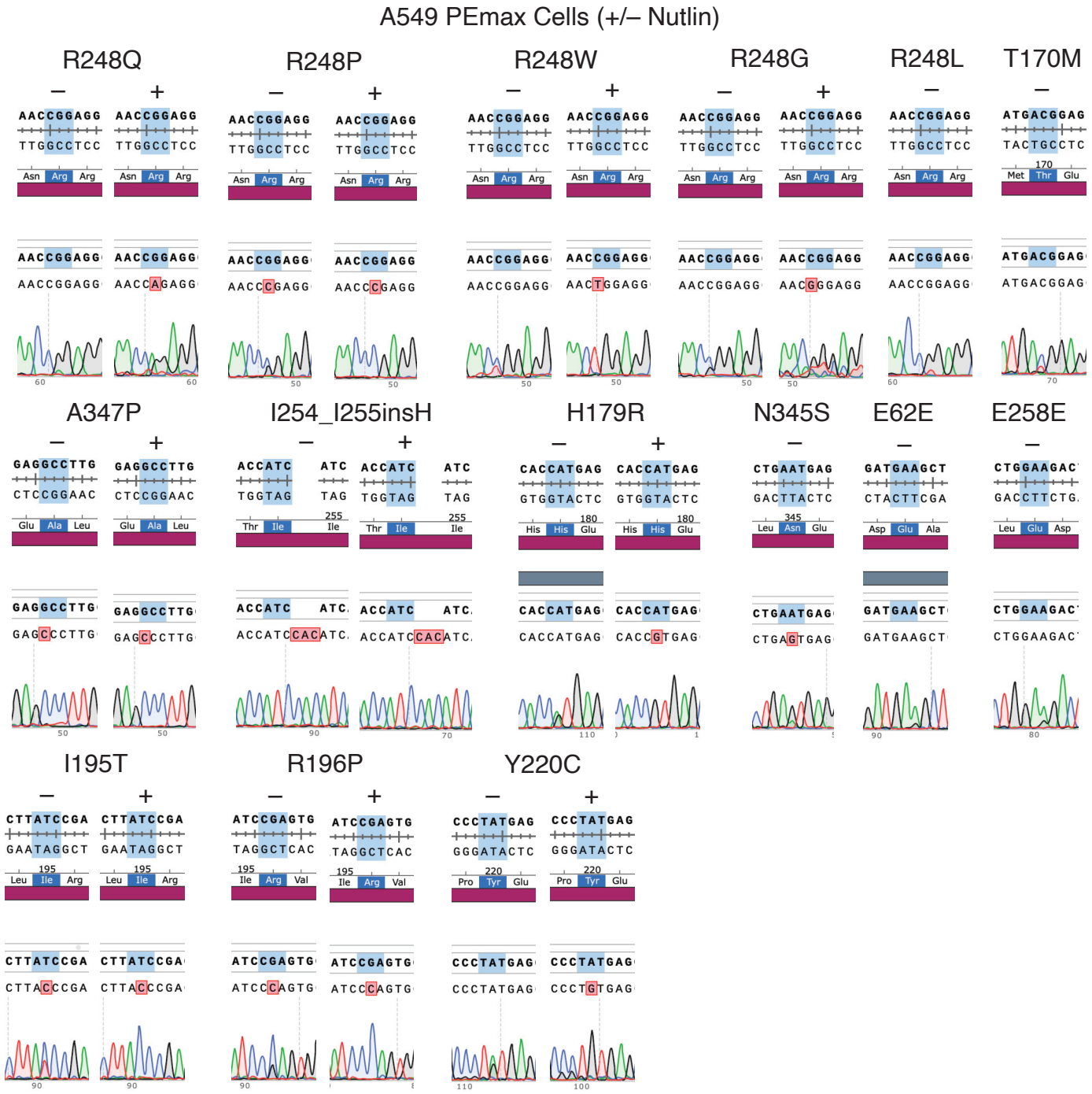

Extended Data Fig. 7 | Endogenous sequencing of TP53 validates the on-target editing activity of individually tested pegRNAs in multiple cell types. Sanger sequencing traces of on-target editing of pure A549-PEmax lines in the presence (+) or absence (-) of Nutlin.

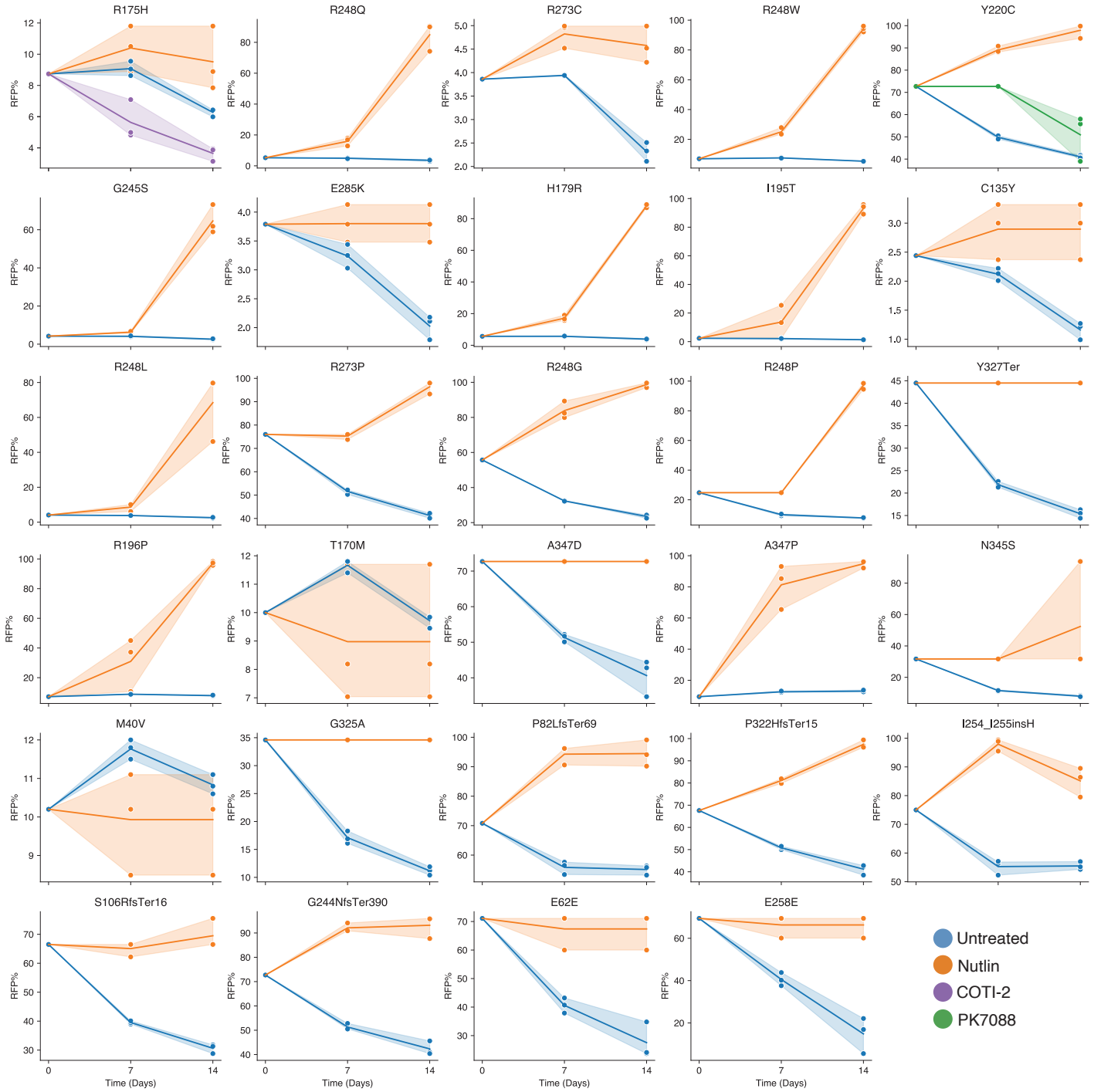

Extended Data Fig. 8 | Competition assays functionally validate the pathogenicity of TP53 variants identified with prime editing screens. Full competition assay plots for each of the 29 pegRNAs chosen for validation. Flow cytometric analyses were performed at days 7 and 14 following the initiation of the competition assay. For data points with fewer than 400 flow cytometry events (indicating insufficient viable cells), the RFP positive percentage was set to be equal to that of the previous time-point.

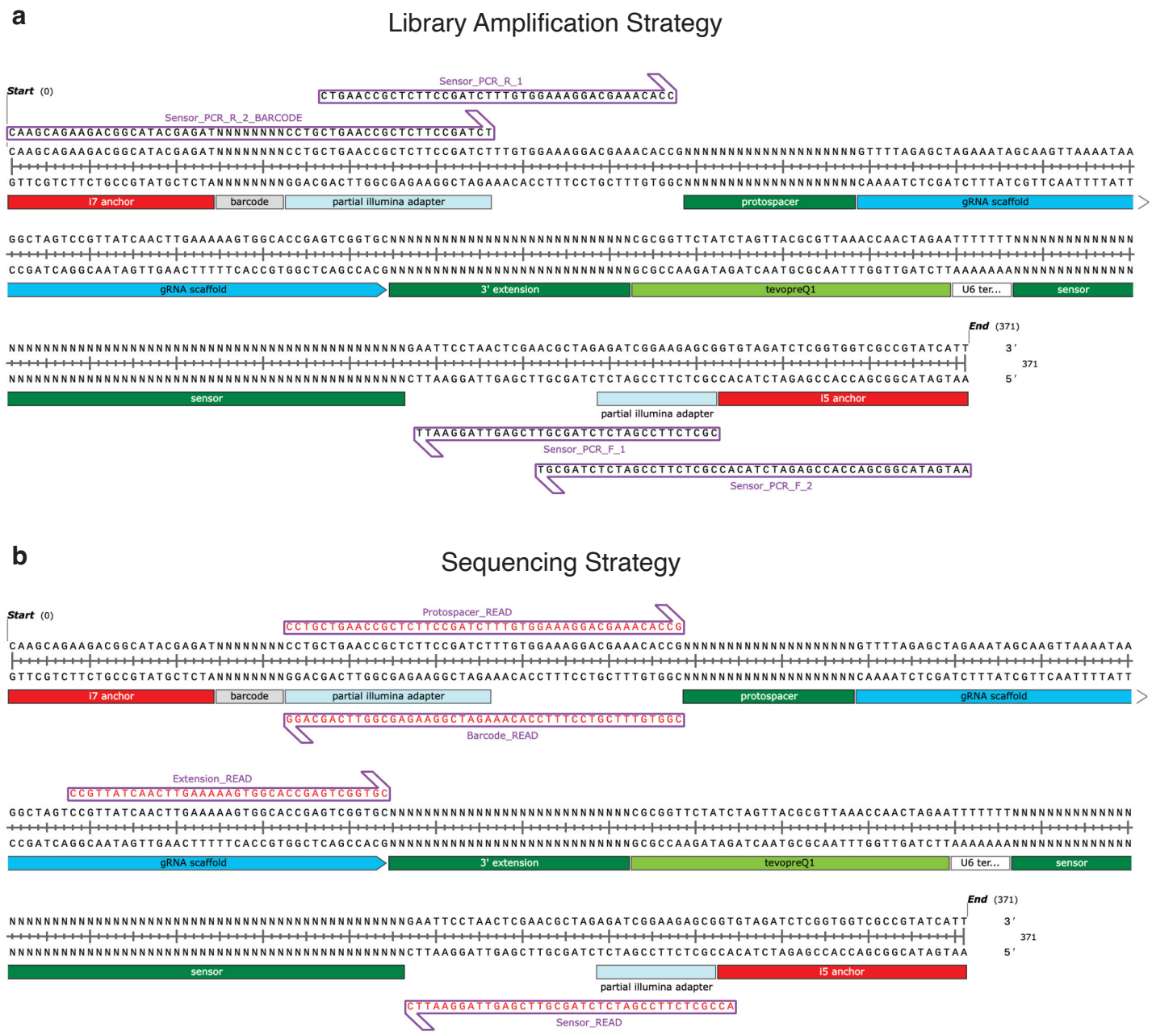

Extended Data Fig. 9 | Library amplification and sequencing strategy. a, Schematic of the PCR1 and PCR2 strategies used to amplify the pegRNA-sensor cassette for NGS. **b,** Custom sequencing strategy used with the NovaSeq 6000 system. Sensor_Read = Read 1, Extension_Read = Read 2, Barcode_Read = index 1 read, Protospacer_Read = index 2 read.